Origin and evolution of Ngaye River alluvial sediments, Northern Cameroon: Geochemical constraints

Paul-Désiré Ndjigui, Anicet Beauvais, Soureiyatou Fadil-Djenabou, Jean-Paul Ambrosi

Mineralogical and geochemical features of the coarse saprolite developed on orthogneiss in the SW of Yaoundé, South Cameroon

P.-D. Ndjigui, M.F.B. Badinane, B. Nyeck, H.P.K. Nandjip, P. Bilong

PII: S1464-343X(12)00225-7
DOI: http://dx.doi.org/10.1016/j.jafrearsci.2012.11.008
Reference: AES 1813

To appear in: *African Earth Sciences*

Received Date: 23 November 2011
Revised Date: 27 August 2012
Accepted Date: 13 November 2012

Please cite this article as: Ndjigui, P.-D., Badinane, M.F.B., Nyeck, B., Nandjip, H.P.K., Bilong, P., Mineralogical and geochemical features of the coarse saprolite developed on orthogneiss in the SW of Yaoundé, South Cameroon, *African Earth Sciences* (2012), doi: http://dx.doi.org/10.1016/j.jafrearsci.2012.11.008

Mineralogical and geochemical features of the coarse saprolite developed on orthogneiss in the SW of Yaoundé, South Cameroon

P.-D. Ndjigui[a,*], M.F.B. Badinane[a], B. Nyeck[a], H.P.K. Nandjip[a], P. Bilong[b]

[a]*Department of Earth Sciences, University of Yaoundé 1, P.O. Box: 812 Yaoundé, Cameroon*

[b]*Faculty of Science, University of Douala, P.O. Box: 24157 Douala, Cameroon*

Corresponding author: lndjigui@yahoo.fr

Abstract

A petrological investigation was performed in the coarse saprolite on orthogneiss in Yaoundé (South Cameroon) using combined whole rock geochemical (XRF, ICP-MS) and mineralogical (XRD, SEM) techniques. The orthogneiss has high contents in SiO_2 (61.56 wt.%), Ba (916 ppm) and REE (209 ppm), moderate content in Al_2O_3 (14.34 wt.%) and negative Eu anomaly ($Eu/Eu^* = 0.68$). The weathering leads to the formation of three main constituents in the coarse saprolite: (i) the loose materials (~85vol.%) are basically clayey silty with relic structure. They are composed of kaolinite, quartz and goethite. The loose materials have high contents in SiO_2 (56 to 64.83 wt.%) and Al_2O_3 (21.48 to 23.96 wt.%), and moderate contents in V (163 to 236 ppm), Ba (95 to 340 ppm) and Zr (160 to 313 ppm). The REE content is low (~ 49 to 169 ppm) relative to the parent rock with LREE-enrichment (LREE/HREE ~ 7 to 17). Positive Ce anomaly ($Ce/Ce^* \sim 3.35$) is observed in the white veins and slight positive Eu anomalies ($Eu/Eu^* \sim 1.2$ to 1.4) are noted in all loose samples. The $(La/Yb)_N$ ratios (~ 0.8 to 1.5) indicate high REE-fractionation. The mass balance calculation reveals the depletion of several elements except Al, Ti, Sc, Y, Th, Sb and Hf; (ii) the iron duricrust (~10vol.%) is located at the bottom and the top of the horizon. The mineral assemblage is dominated by hematite and goethite. The upper iron duricrust has high contents in Fe_2O_3 (45.60 wt.%) and Cr (1641 ppm), moderate contents in V (459 ppm) and Zn (143 ppm), and low REE content (47 ppm) with low LREE/HREE ratio (4.28). The upper iron duricrust is more enriched in Fe_2O_3 (53.26 wt.%) than the lower one. Vanadium, Cr and Zr have high contents relative to other trace elements. The REE content is low (39 ppm) as well as the LREE/HREE ratio (2.94). The iron duricrust has negative Ce anomalies ($Ce/Ce^* \sim 0.66$ to 0.69) and very low $(La/Yb)_N$ ratios (0.1 to 0.3). Several elements reported in the iron duricrust are highly leached except Fe, Cr, Zn, Sc, V, Pb, Zr, Cu and Th; and (iii) the Mn-rich materials (<5vol.%) are made up of birnessite, cryptomelane, and low quantities of quartz,

kaolinite and goethite. The SEM investigation reveals that Ba and Pb are linked in Mn-bearing phases and Ce-oxides appear as fine-grained intergrowth between Mn-bearing phases. The Mn-bearing phases are enriched in MnO (33.86 wt.%), BaO (4.30 wt.%), Co (1716 ppm), Pb (1315 ppm) and Ce (5202 ppm). Positive Ce and Eu anomalies are observed (Ce/Ce^{*} ~ 15.60 and Eu/Eu^{*} ~ 2). The mass balance calculations indicate the strong accumulation of Mn, Ni, Co, Zn, Sc, Cu, Ba, Pb, Y, Ga, Zr and REE. The Mn-bearing phases might be derived from the accumulation of silicate residues and Mn within the parent rock.

The transition from the parent rock to the coarse saprolite is marked by high leaching of several elements.

***Keywords*:** Yaoundé; Orthogneiss; Coarse saprolite; Mineralogy; Geochemistry; Mass balance

1. Introduction

Laterites are the main constituents of weathering mantles in the tropical zone (Mc Farlane, 1976). They are complex materials that derive from the weathering of various rock types (Kamgang Beyala and Ekodeck, 1991; Ndjigui et al., 2008; Etame et al., 2012). Laterites are characterized by large iron duricrust (Beauvais and Colin, 1993; Bitom et al., 2003; Beauvais, 2009). Several works have reported the determination and dating of geochemical fractionation in laterites using U-Th radioactive series (Boulad et al., 1977; Mathieu et al., 1995) or ^{238}U-^{235}U-^{230}Th nuclides (Chabaux et al., 2003). Chabaux and co-workers (2003) highlighted the chemical mobility in the lateritic profile controlled by the iron-cap dismantling. The REE-geochemistry is a useful complementary tool to elucidate chemical variations in geological systems because of their coherent and predictable behaviour (Leybourne et al., 2000). This behaviour combined with their sensitivity to changes in pH, redox conditions and adsorption/desorption reactions, make the rare-earth elements particularly useful as pedogenetic tracers in external geodynamic studies of the earth.

The geochemical characterization has for long been focused on the distribution of major and five or six trace elements in the whole fraction of each soil horizon along the lateritic profile in the Central African rainforest (Ndjigui et al., 1998; Bitom et al., 2003; Nguetnkam et al., 2006). Many works reported since the 90s included the mineralogy and geochemistry of REE in laterites (Braun et al., 1993, 1998; Ndjigui et al., 2008, 2009; Kamgang Kabeyene Beyala et al., 2009). These works have shown that the redox conditions and the nature of the parent rock control the REE distribution in the weathering mantles. They also display an intense REE accumulation in laterites with strong Ce abundance. The lateritic profile is made up, from the bottom to top, of coarse saprolite, fine saprolite, nodular zone and loose clay horizon (Ndjigui et al., 2008). Each soil horizon is made up of numerous plates and patches with different petrophysical, mineralogical and geochemical characteristics. Previous

works on the petrology of major constituents of horizon are very scarce. The Mn-oxide commonly observed is characterized by a fibrous growth texture. It contains Ba and, in few cases, K. This phase can be assigned to either hollandite ($BaMn_8O_{16}$) or cryptomelane (KMn_8O_{16}), which are both isostructural 2:2 tunnel manganates and can contain up to 16 wt.% Ba and 5 wt.% K, respectively, based on the formula (Loges et al., 2012). The behaviour of cerium is complex in the Mn-oxides; Ce has commonly positive anomaly (Koppi et al., 1996; Ohnuki et al., 2008) due to the stability of Ce^{4+} at the oxide surface (Ohta and Kawabe, 2001; Takahashi et al., 2000, 2007). The negative Ce anomaly is rarely observed (Loges et al., 2012). This is due to the strong complexation of Ce^{4+} by siderophores or organic molecules (Davranche et al., 2005, 2008; Loges et al., 2012). At the same time, experimental studies reveal the selective adsorption of REE on kaolinite (Laufer et al., 1984; Coppin et al., 2002). Larger amounts of cerium were adsorbed by natural kaolinite. Cerium may be adsorbed either as a monomeric species or as a polymeric hydroxyl cation (Laufer et al., 1984). In this study, we present detailed mineralogical and geochemical data of three major constituents (loose materials, iron duricrust and Mn-bearing phases) of a coarse saprolite on orthogneiss. The high Ba, Pb and Ce contents in the Mn-bearing phases enabled to determine their stable forms using the microchemistry of the Mn-bearing phases. The last step of this study is the mass balance evaluation of major and trace elements from three main constituents of the coarse saprolite.

2. Geographical and geological setting

The study site is located in the SW of Yaoundé (11°25'-11°30'E and 3°45'-3°50'N; Fig. 1). The climate is humid tropical with four seasons marked by a mean annual temperature of 24°C and an average annual rainfall of 1495 mm (Suchel, 1987). The vegetation corresponds to a transitional zone between rainforest and savannah (Letouzey, 1985). The

morphology of the Yaoundé area (~750 m) is dominated by the smooth-rocky hills with large convex slopes relayed by large swampy valleys. The Yaoundé group constitutes a part of the Central African Mobile Zone (CAMZ) and is pan-African in age (Toteu et al., 2006). Micaschists, quartzites and gneiss occur and are intensively folded (Fig. 1B). The Yaoundé group is made up of two series: the Mbalmayo-Bengbis-Ayos and the Yaoundé series (Maurizot et al., 1986). Paragneiss and orthogneiss are predominant in the Yaoundé series (Fig. 1C). The weathering leads to hillside ferrallitic soils and the swampy hydromorphic soils. The whole swamp is overlain by a grey clayey sandy material with depth varying from 0.5 to 2 m. It is essentially composed of kaolinite and residual quartz, Ti-oxides and zircon grains (Braun et al., 2005).

3. Sampling and analytical techniques

3.1. Sampling techniques

The pit is situated at the hilltop. The weathering profile is 9 m thick and is made up, from the bottom to top, of a coarse saprolite, a fine saprolite, a lower nodular horizon, an iron duricrust horizon, an upper nodular horizon and a loose clayey horizon (Fig. 2). Eleven weathered samples from the coarse saprolite and two rock samples (fresh and slightly weathered) from the outcrop were collected for mineralogical and chemical analyses in the Geoscience Laboratories (Sudbury, Canada).

3.2. Analytical techniques

Thin sections of rocks were observed with an optical microscope (Euromex). Mineralogical analyses were performed on whole rock powders. Powders were prepared by crushing the samples using an agate mortar. Mineral assemblage of rocks and soils was determined using the Panalytical X'Pert Pro. The controlling software is X'Pert data collector,

159 version 2.2h. The analytical conditions are 40 kV and 45 mA. The scan range varies 5 to 85
160 degrees 2 theta and the step size is 0.01. The run time is 8 minutes and 30 seconds/scan. The
161 scanning is continuous and the type of radiation is Co. The mineralogical composition is
162 given in Table 1.

163 Samples were analyzed for major and trace (including lanthanides) elements. They
164 were crushed in an agate mortar and then pulverized in a planetary ball mortar made up of
165 99.8% Al_2O_3. After crushing, the loss on ignition (LOI) was determined. Firstly, the powders
166 were oven-dried at 105°C under nitrogen in order to eliminate water; another sample fraction
167 was heated at 1000°C under oxygen so as to remove the volatile components and oxidize iron.
168 After the determination of the LOI, the major element composition was determined by X-Ray
169 Fluorescence (XRF) with a Panalytical Axios Advanced PW 4400 fluorescence spectrometer.
170 The international reference materials (INTL-09-05401, 09-04868 and 09-04869) and internal
171 laboratory standards (ISHT-09-04204, 09-03903 and 09-03904) were used. Comparisons of
172 measured and reference values are available upon request. The precision of analysis is 5 %.
173 The detection limits and results of major elements are presented in Table 2. Another fraction
174 of the powder was prepared for the trace elements analysis by Inductively Coupled Plasma-
175 Mass Spectrometry (ICP-MS) following the digestion using three acids (see e.g., Burnham
176 and Schweyer, 2004; Ndjigui et al., 2008). The powders were then treated in an acid mixture
177 (HCl and $HClO_4$) at 120°C in a closed container for one week, and then rinsed from their
178 containers with dilute HNO_3 and dried. The residues were dissolved in an acid mixture (HCl
179 and $HClO_4$) and oven-dried for a second time before they were then dissolved in an acid
180 mixture (HNO_3, HCl and HF) at 100°C. The dissolved samples were analyzed in a Perkin
181 Elmer Elan 9000 ICP-MS instrument. The instrumental precision of almost all elements was
182 5% (2σ) for either all or five of the six compiled solutions where the elements were above the
183 limit of quantification. Where the concentrations approached this limit (e.g., for Zr, Ba, La

and Pr in the trace-element poor basalt standard BIR-1, or Eu in the rhyolite standard RGM-1), the error varies between 5 and 8.5% (Burnham and Schweyer, 2004).

Density measurements were carried out in the Department of Earth Sciences of the University of Yaoundé 1 and the results are presented in Table 3. The bulk density (ρ_w) was obtained by the paraffin method. The grain densities (ρ_g) were obtained by the air picnometer method (two replicates). Porosity is calculated using the equation $\phi = [1-(\rho_w/\rho_g)]*100$.

Scanning Electron Microscope (SEM) analysis were carried out at the Geoscience Laboratories using the BSE detector and ED X-ray spectrometer to (i) search for various Mn, Ba, Pb and Ce mineral species due to their high abundances in Mn-bearing phases; and (ii) provide qualitative X-ray data and BSE images of the individual phases. The sample was prepared in three steps: (i) mineral grains and representative pieces of the sample were hand-picked; (ii) several grains were mounted in epoxy plug, polished and carbon coated prior to analysis by SEM; and (iii) several grains were crushed with an agate mortar and pestle, and a smear mount created for XRD analysis. SEM used is a Zeiss EVO 50 and the operating conditions were 20 kV acceleration voltage/1 nA beam current.

4. Results

4.1. Petrology of orthogneiss

The orthogneiss is dark, microbedded and has an augen structure. The rock, with heterogranular grano-lepidoblastic texture, is essentially made up of quartz, biotite, green hornblende, garnet, orthoclase, and accessory microcline, opaque minerals and zircon. The XRD spectra reveal the presence of micas (Table 1). The fresh rock is characterized by high SiO_2, and moderate Al_2O_3, Fe_2O_3, MgO, CaO, K_2O and Na_2O contents (Table 2). The slightly weathered sample is characterized by an increase in SiO_2, Al_2O_3, K_2O, TiO_2 and P_2O_5 contents (Table 2). The bulk density is 2; it is a less porous rock (27.6%, Table 3). The trace

element contents are variable (Table 4). In the fresh rock, elements whose concentrations are more than 100 ppm include Cr, Zn, V, Ba, Zr, Rb and Sr (Table 4). The second category, made up of elements with low concentrations (20 to 90 ppm), include Ni, Cu, Y, Co, Li and Ga. The third category is made up of those whose concentrations are below 19 ppm (Table 4). The chondrite-normalized (McDonough and Sun, 1995) multi-element patterns reveal that orthogneiss and their weathered products are depleted in Co, Ni and Cr contrary to several trace elements (Fig. 3). The total REE content is 209 ppm (Table 4). The elements whose concentrations are high (>40 ppm) include La (43.04 ppm), Ce (87.02 ppm) and Nd (40.79 ppm) (Table 5). The orthogneiss is more enriched in LREE (LREE/HREE ~ 10). The chondrite-normalized REE spectra reveal: (i) strong LREE-enrichment; (ii) slight HREE-enrichment; and (iii) moderate negative Eu anomaly (Eu/Eu^{*} = 0.68) (Fig. 4). The $(La/Yb)_N$ ratios are very high (13.19).

4.2. Petrology of the coarse saprolite

4.2.1. Morphology, mineralogy and distribution of major elements

The coarse saprolite is 2.50 m thick **(**Fig. 2**)**, with a microbedded structure inherited from the parent rock. It is mainly violet red, silty and interspersed with plates of variable colour and texture.

The bottom is made up of a brown material and white veins. The brown material (~80 vol.%) is organized in horizontal, mm-sized, red, grey yellow or white layers. The mineral assemblage is comprised of kaolinite, quartz, goethite, anatase and accessory hematite (Table 1). This material shows high contents in Al_2O_3 (22.48 wt.%) and TiO_2 (1.36 wt.%) relative to the orthogneiss (Table 2). The Fe_2O_3, MnO, MgO, CaO, Na_2O and K_2O contents decrease strongly from the parent rock to the brown material (Table 2). The white veins occur inside the brown material. They are cm-thick, sandy clayey and oriented parallel to the brown

material. Kaolinite and quartz are the dominated minerals (Table 1). Slight increase of contents in SiO_2 (64.83 wt.%), Al_2O_3 (22.76 wt.%) and TiO_2 (1.46 wt.%) is observed relative to the orthogneiss (Table 2).

The whole fraction of the bottom shows a similar mineralogy and geochemistry like the brown material (Tables 1-2).

The upper part is mainly yellowish brown, clayey silty and microbedded. The whole fraction has practically the same mineralogy and geochemistry like the brown material (Tables 1-2). It embeds numerous plates like dark red iron duricrust, black plates, yellowish brown plates and dusky red iron duricrust.

The dark red iron duricrust is fusiform (2 to 3 m long and 0.5 m wide), and includes piled up concentric and cm-layers. It is surrounded by the yellowish brown plate (Fig. 2). The mineral assemblage is made up of hematite, goethite, and few amounts of kaolinite, quartz and anatase (Table 1). The Fe_2O_3 content is 53.26 wt.% and those of SiO_2 and Al_2O_3 are 26.7 and 10.04 wt.%, respectively.

The black phases (~5vol.%) form cm- to dm-sized lobe-shape. They are porous and very hardened materials. They are made up of birnessite, cryptomelane, with accessory quartz, kaolinite and goethite (Table 1). The X-ray diffraction data of selected grains confirms the presence of the birnessite and cryptomelane groups (Fig. 5). The Mn-bearing phases are very enriched in Mn (33.86 wt.%), and depleted in SiO_2 (27.97 wt.%) and Al_2O_3 (12.16 wt.%). The Fe_2O_3 content is quite high (10.08 wt.%) as well as those of other major elements (Table 2).

The yellowish brown plates are disseminated with variable shapes and sizes. They are composed of kaolinite, quartz, goethite and few amounts of rutile and anatase (Table 1). The chemical composition is very close to the uppermost part whole fraction one (Table 2).

The upper boundary of the coarse saprolite is also marked by the presence of dusky red iron duricrust. It is made up of flattened and lobular, interconnected and millimetric plates. The X-ray diffraction data show that hematite and goethite are dominantly associated with few amounts of quartz, kaolinite and anatase (Table 1). The dusky red iron duricrust have high content in Fe_2O_3 (45.60 wt.%) and moderate contents in SiO_2 (30.79 wt.%) and Al_2O_3 (11.90 wt.%).

The bulk density values range between 0.9 and 2.53 (Table 3). The high values are measured in the lower iron duricrust (2.53) and in the Mn-bearing phases (2.36). The upper iron duricrust is less dense (1.66). The loose materials have low density (0.93-1.42) and moderate porosity (35-50%).

4.2.2. Distribution of trace elements

Trace element behaviour was subdivided into five groups according to the periodic table of elements:

a) - alkaline (Li, Rb, Cs) and alkali-earth (Be, Sr, Ba) contents are very low in the loose samples and iron duricrust compared with the parent rock (Table 4). Lithium, Rb, Sr and Ba contents are high in Mn-bearing phases (Table 4);

b) - scandium, V, Cr, Co, Ni and Cu contents are low, except Cr (1641 ppm) and V (459 ppm) in the upper iron duricrust and Co (1716 ppm) in the Mn-bearing phases (Table 4). Other elements also show high contents in Mn-bearing phases (Table 4);

c) - yttrium, Nb, Mo, Hf and W show low concentrations except Zr (Table 4). The Zr contents vary from 83 to 316 ppm; the lowest content occurs in the upper iron duricrust and the highest one is observed in the white veins. Other trace elements of this series have high contents in the Mn-bearing phases (Table 4);

282 d) - other metals (Ga, Zn, Cd, In, Sn, Sb, Tl and Pb) show a similar behaviour like
283 those of the previous groups **(**Table 4). Elements which show high contents include Pb (1315
284 ppm) and Zn (242 ppm) in the Mn-bearing phases;
285 e) - thorium contents range between 5 and 42 ppm. The upper iron duricrust and white
286 veins have highest Th contents, 42.50 and 32.66 ppm, respectively. The lowest Th contents
287 are measured in the Mn-bearing phases (5.8 ppm). A slight increase of uranium contents is
288 observed from the parent rock (1.52 ppm) to the weathered samples (ranging from 1.75 to
289 3.76 ppm) (Table 4).
290
291 *4.2.3. Correlations*
292 The SiO_2/Al_2O_3 and Fe_2O_3/K_2O ratios show that Si and Fe are most abundant than Al
293 and K (Table 2). The Th/U and Th/Co ratios show that orthogneiss and their weathered
294 products are more enriched in Th than U and Co (Table 4). The parent rock-normalized multi-
295 element patterns show strong negative Rb anomalies (Fig. 6). The Harker diagrams show that
296 SiO_2 has positive correlations with Al_2O_3, TiO_2, P_2O_5, Y and U (Fig. 7). However,
297 correlations of SiO_2 with Fe_2O_3, Zr, Cr and V are negative. K_2O, Rb and Th have no
298 significant correlations with SiO_2 (Fig. 7). The binary diagrams show that Fe_2O_3 has a similar
299 trend with ferromagnesian trace elements (Fig. 8). Figure 9 shows (i) strong positive
300 correlations of Zr with Hf, Nb and U; (ii) negative correlations of Zr with Y and Mo; and (iii)
301 any correlation between Zr and Th.
302
303 *4.2.4. Behaviour of rare-earth elements*
304 The total REE content varies between 39 and 5633 ppm (Table 5). The high value is
305 measured in the Mn-phases. The REE content is higher than 100 ppm in two samples and
306 varies from 49 to 96 ppm in several loose samples (Table 5). Both iron duricrust samples have

very low REE content, ranging from 39 to 47 ppm. All the weathered samples highlight LREE-enrichment (LREE/HREE ~ 3 to 86). LREE have strong positive correlations with HREE (Fig. 10).

Overall, the high concentrated REE include La, Ce, Pr, Nd, Sm, Gd and Dy (Table 5).

The binary diagrams reveal that Zr and Pb have strong positive correlations with Ce (Fig. 11A-B). Cerium reveals positive correlation with LREE and REE (Fig. 11C-D). The Ce content influences the behaviour of the bulk LREE and REE. The sum of three lanthanide (La, Ce and Nd) contents is moderate to high, ranging from 30 to 5408 ppm. Lanthanum, cerium and neodymium are the most abundant REE. The binary diagram (La+Ce+Nd) vs. REE shows strong positive correlation of three LREE (La, Ce and Nd) with REE (Fig. 11E). Europium shows a moderate positive correlation with Sr (Fig. 11F).

The parent rock-normalized patterns reveal (Fig. 12A; Table 5): (i) similar behaviour of REE except in the Mn-bearing phases; (ii) slight LREE-depletion; (iii) strong positive Ce and Eu anomalies in Mn-bearing phases (Ce/Ce^{*} = 15.57 and Eu/Eu^{*} = 2.01); (iv) positive Ce anomaly in white veins (Ce/Ce^{*} = 3.35); and (v) moderate negative Ce (Ce/Ce^{*} ~ 0.66 to 0.86) and weak positive Eu anomalies (Eu/Eu^{*} ~ 1.18 to 1.40) in the loose materials and in the iron duricrust. The chondrite-normalized (McDonough and Sun, 1995) patterns reveal the similar trend like the parent rock-normalized spectra (Fig. 12 B). The $(La/Yb)_N$ ratios range between 0.12 and 1.63 (Table 5).

4.2.5. SEM analysis of Mn-phases

The SEM analysis is initiated to understand the distribution of several elements with high concentrations like Mn, Pb, Ba and Ce inside the Mn-rich materials. Under SEM, the Mn-rich material has concentric structure (Figs. 13-14). Barium is detected in all Mn-bearing phases that were analyzed from numerous pieces of the sample. Kaolinite is also detected in

the Mn-bearing phases with Al/Si ratio ~ 1 (Fig. 13). In addition, the atomic ratio of Ba/K is always >1 suggesting that the cryptomelane component could be termed ‘’hollandite’’. The ‘’typical’’ birnessite type composition using the SEM is not identified; the birnessite structure in this case also contains significant Ba, where the ratio of Ba/K also exceeds 1. Cyclical growth patterns are evident in the sample (Fig. 13). The SEM investigation also reveals a much less abundant Pb bearing Mn-phase, perhaps the corandite member of the cryptomelane group. Ce-oxide phase is also relatively common in this sample. In some cases, it forms a rim around the sample or is contained between the apparent growth rings (Fig. 14). There appears to be a fine grained intergrowth between the Mn-bearing phase and an aluminosilicate mineral with a stoichiometry that is consistent with kaolinite (Figs. 14-15).

4.3. Mass balance calculation

The mass balance calculation is a method that enables one to confirm the mobility of chemical elements during weathering. This is done by the estimation of losses or gains of matter expressed either in per cent or kg/m^3 of the weathered parent material. The method currently used takes into account the concentrations, the bulk density and the volume (Brimhall and Dietrich, 1987; Colin and Ambrosi, 1993; Mungall and Martin, 1994; Beauvais, 1999; Cornu et al, 1999; Moroni et al., 2001; Tollari et al., 2008). This method enables one to estimate the quantity of each element which is depleted or accumulated (Colin et al., 1993). This approach can be summarized by the following equations:

The first equation is that of Millot and Bonifas (1955), improved by Brimhall and Dietrich (1987):

$$K_{jm} = \{((C_{jw} \times \rho_w)/(C_{jp} \times \rho_p)) - 1\} \times 100 \quad (1)$$

where K_{jm} is the enrichment or depletion factor, C_{jw} is the concentration of the element *j* in the weathered material *w*, C_{jp} is the concentration of the element *j* in the fresh rock *p*, ρ_{jw} is the bulk density of the weathered material *w*, and ρ_{jp} is the bulk density of the parent rock *p*.

The total mass m_{jw} of each chemical element is obtained through the application of the following equation by Colin et al. (1993):

$$m_{jw} = C_{jp}\,\rho_p\,V_p\,K_{jm} \qquad (2)$$

where m_{jw} is in kg, C_{jp} is the concentration of the element *j* in the parent rock in mg/kg, ρ_p is the bulk density of the parent rock in 10^3 kg/m^3, V_p is the volume of the parent rock in m^3 (Vp = 1 m^3), K_{jm} is the enrichment or depletion factor of the element *j* in the weathered material *w*.

Equation #2 gives the mass *m* (in kg or g) of each element that is transferred per unit volume of the parent rock during the weathering.

The application of the previous equations leads to results presented in Tables 6, 7, 8, 9, 10 and 11. The mass balance calculations reveal a clear disparity in the behaviour of elements in the coarse saprolite.

4.3.1. Relative element mobility

The relative mobility of major elements enables one to classify them into four categories (Table 7): (i) the strongly depleted elements (depletion rate > 90%) such as Mn, alkaline and alkali-earths, and P; (ii) the second category is made up of moderately leached elements (leaching rate ~ 50%) such as Fe and Si; (iii) the third category is made up of weakly leached elements such as Al and Ti; and (iv) the fourth category is that of moderately leached elements to strongly accumulated elements in several materials notably Fe in the iron duricrust, Mn in the Mn-bearing phases and Ti in some loose samples from the top of the coarse saprolite.

Trace elements display a high mobility compared to the major elements. The notable accumulation is found within Mn-bearing phases with more than ten elements (Table 8). Three or four trace elements are accumulated in most samples from the upper part of the coarse saprolite. In all, trace elements are leached from this horizon (Table 8).

The behaviour of REE is very close to that of trace elements. Lanthanides are strongly depleted (rate > 60%) except in the Mn-bearing phases (Table 9).

4.3.2. Mass balance calculation

The weathering of 1 m^3 of orthogneiss into coarse saprolite indicates: (i) strong depletion of an important quantity of Si (400 to 726 kg); (ii) low accumulation of Al in the whole fraction from the upper part (17.85 kg), in the yellowish brown plates (24.45 and 14.05 kg); (iii) more pronounced depletion of Fe than Al (Table 9). However, Fe is strongly accumulated in the Mn-bearing phases (95.98 kg), in the iron duricrust from the bottom (1205 kg) and from the top (615.05 kg); (iv) high Mn accumulation in the Mn-bearing phases (796.48 kg) and leaching of Mn in several samples (Table 9); (v) strong depletion of alkaline and alkali-earth elements (Table 9); (vi) moderate Ti and P depletion; (vii) accumulation of Ti in the upper whole fraction (1.31 kg), in the lower iron duricrust (1.44 kg), and in loose materials (Table 9); (viii) relative accumulation of Pb, Zr, Th, Hf, Sc, V and U in several loose samples (Table 10); (ix) relative accumulation of Zn, Sc, V, Pb, Th, U, Cr, Zn, Cu and Zr in the iron duricrust (Table 10); (xi) accumulation of Ba, Co, Pb, Ni, Zn, Sc, Cu, V, Y, Ga, U, Zr, Sb, Hf, Cd, Mo and Tl in the Mn-bearing phases (Table 10); (xii) high REE-enrichment in the Mn-bearing phases particularly Ce (Table 11); and (xiii) high REE-depletion in almost all the weathered samples (Table 11).

5. Discussion

5.1. Petrology of orthogneiss

The mineralogy and geochemistry indicate that orthogneiss are derived from plutonic rocks. These plutonic rocks might be heterogeneous and characterized by a very variable chemistry. The increase of porosity from the fresh rock to the slightly weathered one might be the result of the dissolution of primary minerals. In the slightly weathered rock, the slight increase in K_2O is due to adsorption and the increase in Al_2O_3 is due to the silicate dissolution. The total moderate REE content might be due to the low proportion of primary REE-bearing minerals (allanite, monazite, xenotime and apatite) in the gneissic formations of South Cameroon (Braun et al., 1998). The negative Eu anomaly could be due to the partial dissolution of feldspars (Gromet and Silver, 1983; Panahi et al., 2000).

5.2. Petrology of the coarse saprolite

5.2.1. Morphology, mineralogy and distribution of major elements

The presence of several phases in the coarse saprolite reveals that the high degree of weathering favours the thinning out of the large microbedded layers observed at the bottom. The mineralogical composition reveals two mineral phases: (i) the first one is composed of kaolinite, goethite, quartz, gibbsite, hematite and anatase. Kaolinite, goethite and gibbsite are characteristic of the well-drained environments in the rainforest region (Nguetnkam et al., 2006). The high quartz proportion is related to acid nature of the parent rock, as well as its slow dissolution during weathering. Goethite might be related to the high porosity that seemingly facilitates the stagnation of water in cavities. It has already been strongly documented that goethite is the main Fe-hydroxide that crystallizes in the saprolite zone (Tardy, 1993; Delvigne, 1998). Hematite results from the dehydration of goethite (Tardy, 1993); and (ii) the second mineral phase is mainly manganiferous. It is characteristic of Mn-

rich materials which might derive directly from the accumulation of silicate residues and Mn within the parent rock (Bourgauth and Rabenhorst, 2011). The presence of the concentric structures could result from successive centripetal reorganizations (Beauvais and Nahon, 1985).

The high SiO_2 contents might be related to the low degree of quartz dissolution (predominant mineral in these samples) in the rainforest zone (Nandjip, 2010). The sharp drop in the concentrations of alkaline and alkali-earth elements might be linked to a rapid dissolution of carrier minerals. The increase in aluminium contents might be correlated with an intense weathering and formation of kaolinite. High Mn contents have been noted in the lower horizons of Ni-laterites in New Caledonia (Golightly, 1979; Llorca and Monchoux, 1991; Traoré, 2005). The positive correlations of SiO_2 with Al_2O_3, TiO_2, P_2O_5, Y and U confirm that Si and Al are the main constituents of silicate residues. At the same time, Ti, P, Y and U might be associated with the relic minerals. The negative correlation between SiO_2 and Fe_2O_3 is due to the weathering of ferromagnesian primary minerals (e.g., biotite, green hornblende) and the formation of goethite and hematite.

5.2.2. Trace elements

The behaviour of trace elements is also dependent on the nature of weathered phases. The Mn-phases are characterized by their high contents in more than ten trace elements including Ni, Co, Zn, Cu, Ba, Pb, Y, Li, Cd, Mo and Tl. These highly concentrated elements might have been adsorbed by precipitation in the interlayer spaces of Mn-oxides (Brindley and Brown, 1980; Mishra et al., 2007). The high Cd contents are related to its fixation by adsorption on kaolinite (Vasconcelos et al., 2008). The highest Cr contents observed in the upper iron duricrust result from relative Cr accumulation as mineral species that were not identified by X-ray diffraction or from their incorporation in the lattice of goethite (Singh et

al., 2002). The negative Nb anomalies confirm the high mobilization of Nb during weathering. The correlation between Fe_2O_3 and ferromagnesian trace elements reveals that ferromagnesian trace elements could be fixed by adsorption on goethite. Both positive correlations (Zr vs. Hf, Nb vs. U) show that Zr, Hf, Nb and U could be hosted by the same minerals such as zircon. The flat signature between Zr and Th shows that zircon is not probably the main Th-bearer.

5.2.3. Rare-earth elements

The low REE content in the loose materials and iron duricrust are characteristic of the weathered materials developed on acidic parent rock (Kamgang Kabeyene Beyala et al., 2009). This might be due to the rapid dissolution of REE-bearers (Braun et al., 1998). Meanwhile, the LREE-enrichment is inherited from the parent rock; this could be also due to the formation of secondary LREE-bearers such as rhabdophane ($LREEPO_4.nH_2O$) (Braun et al., 1998). Braun and co-workers (1998) have reported that xenotime is the major HREE-bearer in gneiss; the low HREE content in the coarse saprolite is controlled by the dissolution of xenotime. The REE content in the Mn-bearing phases is very high (5632 ppm) as compared to those of the parent rock (209 ppm) and other weathered samples (ΣREE is 39-169 ppm). The formation and distribution of secondary minerals have an effect on the REE distribution (Harlavan et al., 2009). The positive correlation of HREE with LREE confirms the coherent behaviour of REE in the coarse saprolite. The positive correlation of the sum of three lanthanide (La, Ce and Nd) contents with the total REE content confirms the prevalence of La, Ce and Nd inside REE. The high Ce content (5202 ppm) in the Mn-bearing phases is due to the stronger sorption of Ce^{4+} or to the probable Ce precipitation as cerianite (CeO_2) onto Mn-hydroxides (Huang and Wang, 2004; Laveuf and Cornu, 2010; this study). The strong positive Ce anomaly results from the lower mobility of Ce^{4+} than REE^{3+} (Yoshida et al., 2004;

Tanaka et al., 2010). This positive Ce anomaly is commonly observed in manganese oxides (Koppi et al., 1996; Ohnuki et al., 2008; Feng, 2010). Also, positive Ce anomaly in the kaolinitic white veins indicates that Ce might have been retained by adsorption into the intracellular crystals of kaolinite (Coppin et al., 2002; Vasconcelos et al., 2008). Laufer and co-workers (1984) have shown that Ce (IV) forms several hydroxyl complexes such as $[Ce(OH)]^{3+}$ and $[Ce(OH)_2]^{2+}$. The number of hydroxyls which are coordinated to Ce depends on the pH and the age of the solution (Laufer et al., 1984). The negative Ce anomalies in several samples show that cerium exists in trivalent form as other REE^{3+} (Marsh, 1990; Leybourne et al., 2000; Ndjigui et al., 2009). The positive Eu anomalies might be due to either the dissolution of feldspars or to other supergene mechanism. Europium might partially substitute Ca^{2+} and Sr^{2+} in feldspars (Gromet and Silver, 1983; Panahi et al., 2000). The proportion of relic primary minerals (e.g.: feldspars, zircon) and secondary minerals (e.g.: kaolinite, goethite) control the major and trace element distribution (Dequencey et al., 2006).

5.2.4. Mass balance calculation

The high leaching of major elements might be related to the primary mineral weathering. The dissolution of feldspars in alkaline granites of NW Spain leads to considerable losses in Si, Na, Ca, K, Rb, Cs, Ba, U and P (Galán et al., 2007). The accumulation of Al, Ti and Fe is reported in the saprolite developed on granodioritic gneiss of Southern India (Tripathi and Rajamani, 2007) or on serpentinite in the South-East Cameroon (Ndjigui et al., 2008; Lambiv Dzemua et al., 2011). The Al accumulation might be due to the fact that aluminium is included within kaolinite. Those of Fe in the iron duricrust suggest an autochthonous origin by leaching of the uppermost ferruginous horizon (Dequencey et al., 2002). The mobility of trace elements is intimately related to the weathering. The high REE-depletion might be linked to the dissolution of REE-bearers (Boulangé and Colin, 1994).

6. Conclusion

This study enables us to understand the mobilization and redistribution of major and trace elements inside the variegated coarse saprolite represented by three main constituents:

1) - loose materials have simple mineral assemblage (quartz, kaolinite and goethite) and slight positive Eu anomalies. However, strong positive Ce anomaly is observed in the kaolinitic white veins;

2) - iron duricrsut is hematitic and goethitic with negative Ce and positive Eu anomalies;

3) - Mn-bearing phases are dominated by birnessite and cryptomelane groups. They show: (i) higher Mn and trace element contents than other weathered samples; (ii) high REE abundance; and (iii) strong positive Ce and Eu anomalies. Ce-oxides appear as fine grained in the Mn-bearing phases.

Weathering helps in accumulation of Al and Ti in the loose samples and numerous elements (Fe, Mn, Cr, Ni, Co, Zn, Sc, Cu, V, Ba, Pb, Y, Ga, Zr, Th and Tl) in the iron duricrust and Mn-bearing phases. This study shows that the nature and the proportion of weathered phases have a prominent influence on the horizon mineralogical and geochemical budget.

Acknowledgements

This work was partially supported by the Geoscience Laboratories (Sudbury, Canada) from the stages of sample preparation to laboratory analysis; we wish to thank Clement Merilla, John Hechler and Dave Crabtree for the SEM observations. The authors gratefully acknowledge the editor and two anonymous reviewers for their detailed comments that have considerably improved the manuscript.

530 **References**

531 Beauvais, A., 1999. Geochemical balance of lateritization processes and climatic signatures in
532 weathering profiles overlain by ferricretes in Central Africa. Geochimica et Cosmochimica
533 Acta 63 (23/24), 3939-3957.

534 Beauvais, A., 2009. Ferricrete biochemical degradation on the rainforest-savannas boundary
535 of Central African Republic. Geoderma 150, 379-388.

536 Beauvais, A., Colin, F., 1993. Formation and transformation processes of iron duricrust
537 systems in tropical humid environment. Chemical Geology 106, 77-101.

538 Beauvais, A., Nahon, D., 1985. Nodules and pisolites from manganiferous weathering profiles
539 under lateritic influences. Examples from Ivory Coast and Gabon. Bulletin Sciences
540 Géologiques 38 (4), 359-381.

541 Bitom, D., Volkoff, B., Angue-Abossolo, M., 2003. Evolution and alteration in situ of a
542 massive iron duricrust in Central Africa. Journal of African Earth Sciences 37, 89-101.

543 Boulad, A.P., Muller, J.-P., Bocquier, G., 1977. Essai de détermination de l'âge et de la
544 vitesse d'altération d'un sol ferrallitique camerounais à l'aide de la méthode du déséquilibre
545 radioactif uranium/thorium. Bulletin Sciences Géologiques 30, 175-188.

546 Boulangé, B., Colin, F., 1994. Rare earth element mobility during conversion of nepheline
547 syenite into lateritic bauxite at Passa Quatro. Minais Gerais, Brazil. Applied Geochemistry 9,
548 701-711.

549 Bourgauth, R.R., Rabenhorst, M.C., 2011. Genesis and characterization of manganiferous
550 soils in the Eastern Piedmont, USA. Geoderma 165(1), 84-94.

551 Braun, J.-J., Ndam Ngoupayou J.R., Viers, J., Dupre, B., Bedimo Bedimo J.-P., Boeglin, J.-
552 L., Robain, H., Nyeck, B., Freydier, R., Sigha Nkamdjou, L., Rouiller, J., Muller, J.-P., 2005.
553 Present weathering rates in a humid tropical watershed: Nsimi, South Cameroon. Geochimica
554 et Cosmochimica Acta 69, 357-387.

555 Braun, J.-J., Pagel, M., Herbillon, A., Rosin, C., 1993. Mobilization and redistribution of
556 REEs and Th in syenitic lateritic profile: - a mass-balance study. Geochimica et
557 Cosmochimica Acta 57, 4419-4434.
558 Braun, J.-J., Viers, J., Dupre, B.,Polve, M., Ndam, J., Muller, J.-P., 1998. Solid/liquid REE
559 fractionation in the lateritic system of Goyoum, East Cameroon: the implication for the
560 present dynamics of the soil covers of the humid tropical regions. Geochimica et
561 Cosmochimica Acta 62, 273-299.
562 Brimhall, G.H., Dietrich, W.E., 1987. Constitutive mass-balance relations between chemical
563 composition, volume, density, porosity and strain in metasomatic hydrochemical systems:
564 results on weathering and pedogenesis. Geochimica et Cosmochimica Acta 51, 567-587.
565 Brindley, G.W., Brown, G., 1980. Crystal structures of clay minerals and their x-ray
566 identification. Mineralogical Society, London, p. 495.
567 Burnham, O.M., Schweyer, J., 2004. Trace element analysis of geological samples by
568 inductively Coupled Plasma Mass Spectrometry at the Geoscience Laboratories: revised
569 capabilities due to improvements to instrumentation. Summary of Field Work and Other
570 Activities 2004, Ontario Geological Survey, Open file report 6145, 54, 1-20.
571 Chabaux, F., Dequincey, O., Lévèque, J.-J., Leprun, J.-C., Clauer, N., Riotte, J., Paquet, H.,
572 2003. Tracing and dating recent chemical transfers in weathering profiles by trace-element
573 geochemistry and ^{238}U-^{234}U-^{230}Th disequilibria: the example of the Kaya lateritic
574 toposequence (Burkina-Faso). C.R. Geoscience 335, 1219-1231.
575 Colin, F., Ambrosi, J.-P., 1993. Gold mass transfer during lateritic weathering under
576 equatorial rainforest conditions. Chemical Geology 107, 285-288.
577 Colin, F., Veillard, P., Ambrosi, J.-P., 1993. Quantitative approach to physical and chemical
578 gold mobility in equatorial rainforest lateritic environment. Earth Planetary Science Letters
579 114, 269-285.

580 Coppin, F., Berger, G., Bauer, A., Castet, S., Loubet, M., 2002. Sorption of lanthanides on
581 smectite and kaolinite. Chemical Geology 182, 57-68.
582 Cornu, S., Lucas, Y., Lebon, E., Ambrosi, J.-P., Luizão, F., Rouiller, J., Bonnay, M., Neal, C.,
583 1999. Evidence of titanium mobility in soil profiles. Manaus, Central Amazonia. Geoderma
584 91, 281-295.
585 Davranche, M., Pourret, O., Gruau, G., Dia, A., Jin, D., Gaertner, D., 2008. Competitive
586 binding of REE to humic acid and manganese oxide: impact of reaction kinetics on
587 development of cerium anomaly and REE adsorption. Chemical Geology 247, 154-170.
588 Davranche, M., Pourret, O., Gruau, G., Dia, A., Le Coz-Bouhnik, M., 2005. Adsorption of
589 REE(III)-humate complexes onto MnO_2, experimental evidence for cerium anomaly and
590 lanthanide tetrad effect suppression. Geochimica et Cosmochimica Acta 69, 4825-4835.
591 Delvigne, J.E., 1998. Atlas of micromorphology of mineral alteration and weathering. The
592 Canadian Mineralogist, special publication 3, p. 494.
593 Dequencey, O., Chabaux, F., Clauer, N., Sigmarsson, O., Liewig, N., Leprun, J.-C., 2002.
594 Chemical mobilizations in laterites: Evidence from trace elements and ^{238}U-^{234}U-^{230}Th
595 disequilibria. Geochimica et Cosmochimica Acta 66, 1997-1210.
596 Dequencey, O., Chabaux, F., Leprun, J.-C., Paquet, H., Clauer, N., Larque, P., 2006.
597 Lanthanide and trace element mobilization in a lateritic toposequence: inferences from the
598 Kaya laterite in Burkina Faso. European Journal of Soil Science 57, 816-830.
599 Etame, J., Suh, C.E.,Gerard, M., Bilong, P., 2012. Phillipsite formation in nephelinitic rocks
600 in response to hydrothermal alteration at Mount Etinde, Cameroon. Chemie der Erde-
601 Geochemistry 72, 31-37.
602 Feng, J.L., 2008. Behaviour of rare earth elements and yttrium in ferromanganese concretions,
603 gibbsite spots, and surrounding terra rossa over dolomite during chemical weathering.
604 Chemical Geology 271, 112-132.

605 Galán, E., Fernández-Caliani, J.C., Miras, A., Aparicio, P., Márquez, M.G., 2007. Residence
606 and fractionation of rare earth elements during kaolinization of alkaline peraluminous granites
607 in NW Spain. Clays Minerals 42 (3), 341-352.
608 Golightly, J.-P., 1979. Geology of Soroako nickeliferous laterite deposits. AIME International
609 laterite Symposium, pp. 38-55.
610 Gromet, P.L., Silver, L.T., 1983. Rare earth element distributions among minerals in a
611 granodiorite and their petrogenetic implications. Geochimica et Cosmochimica Acta 47 (5),
612 925-939.
613 Harvalan, Y., Erel, Y., Blum, J.D., 2009. Coupled release of REE and Pb to the soil labile
614 pool with time by weathering of accessory phases, wind river mountains, WY. Geochimica et
615 Cosmochimica Acta 73, 320-336.
616 Huang, C., Wang, C., 2004. Geochemical characteristics and behaviors of rare earth elements
617 in process of vertisol development. Journal of Rare Earths 22 (4), 552-557.
618 Kamgang Beyala, V., Ekodeck, G.E., 1991. Altération et bilans géochimiques des biotites des
619 gneiss de Nkolbisson (NW de Yaoundé, Cameroun). Géodynamique 6 (2), 191-199.
620 Kamgang Kabeyene Beyala, V., Onana V.L., Ndome Effoudou Priso, E., Parisot, J.-C.,
621 Ekodeck, G.E., 2009. Behaviour of REE and mass balance calculations in a lateritic profile
622 over chlorite schists in South Cameroon. Chemie der Erde-Geochemistry 69, 61-73.
623 Koppi, A.J., Edis, R., Field, D.J., Geering, H.R., Klessa, D.A., Cockayne, D.J.H., 1996. Rare
624 earth element trends and cerium-uranium-manganese associations in weathered rock from
625 Koongarra, Northern Territory, Australia. Geochimica et Cosmochimica Acta 60, 1695-1707.
626 Lambiv Dzemua G., Mees F., Stoops G., Van Ranst E., 2011. Micromorphology, mineralogy
627 and geochemistry of lateritic weathering over serpentinite in south-east Cameroon. Journal of
628 African Earth Sciences 60, 38-48.

629 Laufer, F., Yariv, S., Steinberg, M., 1984. The adsorption of quadrivalent cerium by kaolinite.
630 Clay Minerals 19, 137-149.
631 Laveuf, C., Cornu, S., 2010. A review on the potentiality of rare earth elements to trace
632 pedogenetic processes. Geoderma 154, 1-12.
633 Letouzey, R., 1985. Notice explicative de la carte phytogéographique du Cameroun à
634 l'échelle de 1/500 000. Institut de la Carte Internationale de la Végétation, Toulouse, p. 240.
635 Leybourne, M.I., Goodfellow, W.D., Bowle, D.R., Hall, G.M., 2000. Rapid development of
636 negative Ce anomalies in surface waters and contrasting REE patterns in ground waters
637 associated with Zn-Pb massive sulphide deposits. Applied Geochemistry 15, 695-793.
638 Llorca, S., Monchoux, P., 1991. Supergene cobalt minerals from New Caledonia. Canadian
639 Mineralogist 29, 149-161.
640 Loges, A., Wagner, T., Barth, M., Bau, M., Göb, S., Markl, G., 2012. Negative Ce anomalies
641 in Mn oxides: the role of Ce^{4+} mobility during water-mineral interaction. Geochimica et
642 Cosmochimica Acta 86, 296-317.
643 Marsh, J.S., 1990. REE fractionation and Ce anomalies in weathered Karoo dolerite.
644 Chemical Geology 90, 189-194.
645 Mathieu, D., Bernat, M., Nahon, D., 1995. Short-lived U and Th isotope distribution in a
646 tropical laterite derived from granite (Pitinga River Basin, Amazonia, Brazil): application to
647 assessment of weathering rate. Earth Planetary Science Letters 136, 703-714.
648 Maurizot, P., Abessolo, A., Feybesse, A., Johan, V., Lecomte, P., 1986. Etude et prospection
649 minière du Sud-Ouest Cameroun. Synthèse des travaux de 1978 à 1985. 85-CMR 066 BRGM.
650 McDonough, W.F., Sun, S.S., 1995. The composition of the Earth. Chemical Geology 120,
651 223-253.
652 McFarlane, M.J., 1976. Laterite and landscape. Academic Press, London, p. 151.

653 Millot, G., Bonifas, M., 1955. Transformations iso-volumiques dans les phénomènes de
654 latéritisation et de bauxitisation. Bulletin du Service de la Carte Géologique d'Alsace-
655 Lorraine 8, 8-10.
656 Mishra, P.P., Mohapatra, B.K., Singh, P.P., 2007. Contrasting REE signatures on manganese
657 ores of iron ore group in North Orissa, India. Journal of Rare Earths 25, 749-758.
658 Moroni, M., Girardi, V.A.V., Ferrario, A., 2001. The Serra Pelada Au-PGE deposit, Serra dos
659 Cerajás (Pará State, Brazil): geological and geochemical indications for a composite
660 mineralising process. Mineralium Deposita 36, 768-785.
661 Mungall, J.E., Martin, R.F., 1994. Severe leaching of trachyte glass without devitrification,
662 Terceira, Azores. Geochimica et Cosmochimica Acta 58, 75-83.
663 Nandjip K.P.H., 2010. Contribution à l'étude pétrologique d'une isaltérite développée sur
664 orthogneiss au SW de Yaoundé : recherche des indices de cérium dans les matériaux
665 ferruginisés. Master, Univ. de Yaoundé I, p. 70.
666 Ndjigui, P.-D., Bilong, P., Bitom, D., 2009. Negative cerium anomalies in the saprolite zone
667 of serpentinite lateritic profiles in the Lomié ultramafic complex, South-East Cameroon.
668 Journal of African Earth Sciences 53, 59-69.
669 Ndjigui, P.-D., Bilong, P., Bitom, D., Dia, A., 2008. Mobilization and redistribution of major
670 and trace elements in two weathering profiles developed on serpentinite in the Lomié
671 ultramafic complex, South-East Cameroon. Journal of African Earth Sciences 50, 305-328.
672 Ndjigui, P.-D., Bilong, P., Nyeck, B., Eno Belinga, S.-M., Vicat, J.-P., Gérard, M., 1998. Les
673 produits d'altération du gneiss à biotite et amphibole dans la plaine côtière de Douala.
674 Annales Fac. Sci., série Sci. Nat. et Vie, vol. 34, 191-216.
675 Nguetnkam, J.-P., Yongue-Fouateu, R., Bitom, D., Bilong, P., Volkoff, B., 2006. Etude
676 pétrologique d'une formation latéritique sur granite en milieu tropical forestier sud-

677 camerounais (Afrique centrale). Mise en évidence de son caractère polyphasé. Etude et
678 Gestion des Sols 13, 89-102.
679 Ohnuki, T., Ozaki, T., Kozai, N., Nankawa, T., Sakamoto, F., Sakai, T., Suzuki, Y., Francis,
680 A.J., 2008. Concurrent transformation of Ce(III) and formation of biogenic manganese
681 oxides. Chemical Geology 253, 23-29.
682 Ohta, A., Kawabe, I., 2001. REE(III) adsorption onto Mn dioxide (δ-MnO_2) and Fe
683 oxyhydroxide: Ce(III) oxidation by (δ-MnO_2). Geochimica et Cosmochimica Acta 65 (5),
684 695-703.
685 Owona, S., Mvondo Ondoa, J., Essono, J., Tjomb, B., Enama Mengong, M., 2003.
686 Géomorphologie et cartographie de deux faciès paradérivés et un orthodérivé de la région de
687 Yaoundé. Sci. Technol. Dev., Vol. 10 (1), 81-91.
688 Panahi, A., Young, G.M., Rainbird, R.H., 2000. Behavior of major and trace elements
689 (including REE) during Paleoproterozoic pedogenesis and diagenetic alteration of an
690 Archaean granite near Ville Marie, Québec, Canada. Geochimica et Cosmochimica Acta 64
691 (13), 2199-2220.
692 Singh, B., Sherman, D.M., Gilkes, R.J., Wells, M.A., Mosselmans, J.F.W., 2002.
693 Incorporation of Cr, Mn and Ni into goethite (α-FeOOH): mechanism from extended X-ray
694 absorption fine structure spectroscopy. Clay Minerals 37, 636-649.
695 Suchel, J.-B., 1987. Les climats du Cameroun. Thesis, Université de Bordeaux III, p. 1186.
696 Takahashi, Y., Manceau, A., Geoffroy, N., Marcus, M.A., Usui, A., 2007. Chemical and
697 structural control of the partitioning of Co, Ce, and Pb in marine ferromanganese oxides.
698 Geochimica et Cosmochimica Acta 71, 984-1008.
699 Takahashi, Y., Shimizu, H., Usui, H., Kagi, H., Nomura, M., 2000. Direct observation of
700 tetravalent cerium in ferromanganese nodules and crusts by x-ray-absorption near-edge
701 structure (XANES). Geochimica et Cosmochimica Acta 17, 2929-2935.

Tanaka, K., Tani, Y., Takahashi, Y., Tanimizu, M., Suzuki, Y., Kozai, N., Ohnuki, T., 2010. A specific Ce oxidation process during sorption of rare earth elements on biogenic Mn oxide produced by *Acremonium sp.* Strain KR21-2. Geochemica et Cosmochemica Acta 74, 5463-5477.

Tardy, Y., 1993. Pétrologie des latérites et des sols tropicaux. Masson, Paris, p. 459.

Tollari, N., Barnes S.-J., Cox, R.A., Nabil, H., 2008. Trace element concentrations in apatites from the Sept-Îles intrusive suite, Canada – Implications for the genesis of nelsonites. Chemical Geology 252, 180-190.

Toteu, S., Penaye, J., Deloule, E., Van Schmus, W.R., Tchameni, R., 2006. Diachronous evolution of volcano-sedimentary basins north of the Congo craton: insights from U-Pb ion microphobe dating zircon from Poli, Lom and Yaoundé groups (Cameroon). Journal of African Earth Sciences 44, 428-442.

Traoré, D., 2005. Serpentinisation hydrothermale et altération latéritique des roches ultrabasiques en milieu tropical: évolution géochimique et minéralogique de la minéralisation en platine de la rivière des Pirogues (Nouvelle-Calédonie). Thesis, Université de la Nouvelle Calédonie, p. 191.

Tripathi, J.K., Rajamani, V., 2007. Geochemistry and origin of ferruginous nodules in weathered granodioritic gneisses, Mysore Plateau, Southern India. Geochimica et Cosmochimica Acta 71 (7), 1674-1688.

Vasconcelos, I.F., Haack, E.A., Maurice, P.A., Bunker, B.A., 2008. EXAFS analysis of cadmium (II) adsorption to kaolinite. Chemical Geology 249, 237-249.

Yoshida, T., Ozaki, T., Ohnuki, T., Francis, A.J., 2004. Adsorption of rare earth elements by γ-Al_2O_3 and *Pseudomonas fluorescens* cells in the presence of desferrioxamine B: implication of siderophores for the Ce anomaly. Chemical Geology 212, 239-246.

Figure captions

Fig. 1. Location and geological map of Yaoundé. A. Location of Yaoundé; B. Geological map of the SW Cameroon (modified after Maurizot et al., 1986); C. Geological map of the Yaoundé (modified after Owona et al. 2003).

Fig. 2. Macroscopic organization of the weathering profile.

Fig. 3. Chondrite-normalized (McDonough and Sun, 1995) multi-element patterns for orthogneiss and main constituents of the coarse saprolite (for acronyms, see Table 4).

Fig. 4. Chondrite-normalized (McDonough and Sun, 1995) rare-earth element patterns for orthogneiss.

Fig. 5. X-ray diffraction spectra for Mn-bearing phase of several grains from the black plates, indicating good peaks for birnessite and cryptomelane groups, as well as quartz.

Fig. 6. Parent rock-normalized multi-element patterns for the coarse saprolite (for acronyms, see Table 4).

Fig. 7. Harker diagrams of selected major and trace elements.

Fig. 8. Scattergrams of Fe_2O_3 with selected ferromagnesian trace elements: A. Fe_2O_3 vs. Cr; B. Fe_2O_3 vs. Ni; C. Fe_2O_3 vs. Co; D. Fe_2O_3 vs. V.

751 Fig. 9. Scattergrams of Zr with selected trace elements: A. Zirconium vs. vanadium; B.
752 Zirconium vs. hafnium; C. Zirconium vs. niobium; D. Zirconium vs. molybdenum; E.
753 Zirconium vs. thorium; F. Zirconium vs. uranium.
754
755 Fig. 10. Scattergram of light rare-earth elements (LREE) with heavy rare-earth elements
756 (HREE).
757
758 Fig. 11. Scattergrams of selected rare-earth elements with Zr, Pb and rare-earth elements: A.
759 Cerium vs. zirconium; B. Cerium vs. lead; C. Cerium vs. light rare-earth elements; D. Sum of
760 Total rare-earth element (REE) content vs. cerium; E. Three lanthanide (Ce, La and Nd)
761 content vs. total rare-earth element (REE) content; F. Strontium vs. europium.
762
763 Fig. 12. A. Parent rock-normalized rare-earth element patterns for the coarse saprolite. B.
764 Chondrite-normalized (McDonough and Sun, 1995) rare-earth element patterns for the coarse
765 saprolite (for acronyms, see Table 5).
766
767 Fig. 13. BSE image of a grain displaying cyclic growth patterns in sample. The EDS spectra
768 are shown for the Mn-bearing phase (bright contrast) and the aluminosilicate phase (dark-grey
769 contrast). Several Ce-oxides grains (very bright contrast, each approximately 1 to 10 microns
770 in diameter) appear marginal to the sample as indicated.
771
772 Fig. 14. BSE image of the Mn-bearing phase with a blow-out picture of Ce-oxide marginal to
773 the sample (lower left) and a blow-out picture of the Mn-bearing phase intergrowth with the
774 aluminosilicate phase (upper right).
775

776 Fig. 15. BSE image displaying the intergrowth of the Mn-bearing phase with the
777 aluminosilicate phase.

778

779

780 Positive Eu-anomalies in all weathered samples.
781 Negative Ce-anomalies in the loose and iron duricrust samples, and positive one in the
782 kaolinitic white veins.
783 High Mn, Co, Ba, Zr, Pb and Ce contents in the Mn-bearing phases. Strong positive
784 Ce-anomaly is observed.
785 Strong depletion of several elements in the loose and iron duricrust sapmles.

786
787
788

Table 1
Mineralogical composition of the parent rock and the main constituents of the coarse saprolite.

	Parent rock		Coarse saprolite										
	Fresh rock	Sligthly weathered rock	Bottom			Top							
			Whole fraction	Brown material	White veins	Whole fraction	Dark red iron duricrust	Black phases	Yellowish brown plates				Dusky red iron duricrust
									(a)	(b)	(c)	(d)	
Depth (m)	-	-	-	+ 0.10	+ 0.40	-	+1.70	+1.7 0	+1.70	+1.80	+2.10	+2.40	+2.50
Ref. code	CE 01	CE 02	CE 04	CE 07	CE 08	CE 10	CE 09	CE 13	CE 11	CE 12	CE 06	CE 14	CE 05
Micas	++	++	-	-	-	-	-	-	-	-	-	-	-
Plagioclase	++	++	-	-	-	-	-	-	-	-	-	-	-
Green hornblende	+	+	-	-	-	-	-	-	-	-	-	-	-
Garnet	+	+	-	-	-	-	-	-	-	-	-	-	-
Orthose	+	+	-	-	-	-	-	-	-	-	-	-	-
Microcline	ε	ε	-	-	-	-	-	-	-	-	-	-	-
Epidote	ε	ε	-	-	-	-	-	-	-	-	-	-	-
Kaolinite	-	-	+++	+++	+++	+++	+	+	++	+++	+++	+++	+
Quartz	+++	+++	+++	+++	++	+++	+	++	+++	+++	+++	+++	++
Rutile	-	-	-	-	+	-	-	-	-	-	+	-	-
Goethite	-	-	+	+	+	++	+++	+	++	++	++	++	+++
Hematite	-	-	-	ε	ε	-	+++	-	-	-	-	-	+++
Cryptomelane	-	-	-	-	-	-	-	+++	-	-	-	-	-
Birnessite	-	-	-	-	-	-	-	+++	-	-	-	-	-
Anatase	-	-	+	-	+	-	+	-	+	+	-	-	+

+++: very abundant; ++: abundant; +: poorly represented; ε: trace; -: not identified.

Table 2
Major element composition of the parent rock and the main constituents of the coarse saprolite (%wt of oxides).

	d.l.	Parent rock		Coarse saprolite										
				Bottom			Top							
		Fresh material	Sligthly weathered material	Whole fraction	Brown material	White veins	Whole fraction	Dark red iron duricrust	Mn-phases	Yellowish brown plates				Dusky red iron duricrust
										(a)	(b)	(c)	(d)	
Depth (m)	-	-	-	-	+ 0.10	+ 0.40	-	+1.70	+1.7 0	+1.70	+1.80	+2.10	+2.40	+2.50
Ref. code	-	CE 01	CE 02	CE 04	CE 07	CE 08	CE 10	CE 09	CE 13	CE 11	CE 12	CE 06	CE 14	CE 05
SiO_2	0.01	61.56	61.84	61.80	61.25	64.83	58.03	26.70	27.97	56.10	57.01	59.05	60.30	30.79
Al_2O_3	0.01	14.34	15.63	22.34	22.48	22.76	22.18	10.04	12.16	22.02	22.90	23.96	21.48	11.90
Fe_2O_3	0.01	7.06	6.66	5.12	5.41	2.26	7.68	53.26	10.08	8.63	6.46	4.80	6.74	45.60
MnO	0.01	0.13	0.11	0.01	0.01	0.01	0.01	0.01	33.86	0.01	0.01	0.01	0.01	0.01
MgO	0.01	4.40	2.92	<dl	<dl	<dl	0.01	0.04	0.15	0.09	0.08	<dl	0.01	0.04
CaO	0.01	4.71	3.64	0.03	0.02	0.02	0.02	0.02	0.03	0.02	0.02	0.02	0.02	0.02
Na_2O	0.01	2.72	2.58	<dl	<dl	<dl	0.02	<dl	0.11	0.02	0.02	<dl	0.02	<dl
K_2O	0.01	2.81	3.15	0.04	0.03	0.04	0.03	0.01	0.32	0.02	0.02	0.04	0.05	0.01
TiO_2	0.01	0.91	1.07	1.35	1.36	1.46	1.42	0.78	0.16	1.50	1.46	1.52	1.02	0.67
P_2O_5	0.01	0.23	0.28	0.09	0.09	0.08	0.07	0.03	0.03	0.05	0.06	0.10	0.09	0.10
LOI	0.05	0.43	1.64	9.37	9.38	9.23	9.97	8.93	12.41	10.45	10.64	10.17	9.60	10.24
Total	-	99.30	99.52	100.15	100.03	100.69	99.44	99.82	97.28	98.91	98.68	99.67	97.28	99.38
SiO_2/Al_2O_3	-	4.29	3.96	2.77	2.72	2.85	2.62	2.66	2.30	2.55	2.49	2.46	2.81	2.59
Fe_2O_3/K_2O	-	2.51	2.11	1.28	180.33	56.50	256.00	5326.00	31.50	431.50	323.00	120.00	134.80	4560.00

d.l.: detection limits.
Note that the BaO content is 4.30 wt.% in the Mn-phases.
Ref. code: reference code.

Table 3
Bulk density and porosity (in %) of the parent rock and the main constituents of the coarse saprolite.

	Parent rock		Coarse saprolite										
	Fresh rock	Sligthly weathered rock	Bottom			Top							
			Whole fraction	Brown material	White veins	Whole fraction	Dark red iron duricrust	Mn-phases	Yellowish brown plates				Dusky red iron duricrust
									(a)	(b)	(c)	(d)	
Depth (m)	-	-	-	+ 0.10	+ 0.40	-	+1.70	+1.7 0	+1.70	+1.80	+2.10	+2.40	+2.50
Ref. code	CE 01	CE 02	CE 04	CE 07	CE 08	CE 10	CE 09	CE 13	CE 11	CE 12	CE 06	CE 14	CE 05
Bulk density	2.01	2.06	1.28	0.93	1.10	1.38	2.53	2.36	1.42	1.32	1.14	1.29	1.66
Porosity	27.69	25.09	50.38	35.22	46.41	45.01	22.86	27.00	47.00	49.00	51.81	50.00	36.72

Table 4
Trace element composition of the parent rock and the main constituents of the coarse saprolite (ppm).

	d.l.	Parent rock		Coarse saprolite										
		Fresh rock	Sligthly weathered rock	Bottom			Top							
				Whole fraction	Brown material	White veins	Whole fraction	Dark red iron duricrust	Mn-phases	Yellowish brown plates				Dusky red iron duricrust
										(a)	(b)	(c)	(d)	
		CE 01	CE 02	CE 04	CE 07	CE 08	CE 10	CE 09	CE 13	CE 11	CE 12	CE 06	CE 14	CE 05
Cr	3.00	276.30	101.00	309.00	338.00	272.00	367.00	189.00	105.00	341.00	313.00	373.00	238.00	1641
Ni	1.60	84.50	30.30	21.00	20.20	16.30	25.90	33.00	79.80	25.10	24.50	26.60	21.10	18.20
Co	0.13	27.32	15.56	3.05	2.71	2.00	2.66	7.28	1716	2.79	2.20	2.27	3.44	5.37
Zn	7.00	105.00	110.00	40.00	38.00	37.00	54.00	155.00	242.00	62.00	51.00	53.00	53.00	143.00
Sc	1.10	17.60	15.10	23.80	25.10	25.50	26.50	33.80	28.00	28.80	27.00	24.40	24.70	48.80
Cu	1.40	38.30	12.50	18.80	21.30	20.60	37.10	22.90	333.90	43.90	31.40	23.90	34.80	82.10
V	0.80	134.90	123.40	212.10	196.70	190.60	236.80	282.40	126.30	246.80	217.40	233.70	163.20	459.00
Ba	0.80	916.00	871.90	319.60	323.40	311.70	181.70	18.60	51690	95.00	158.20	320.40	340.60	106.30
Pb	0.60	15.30	17.30	25.90	25.50	20.20	21.00	18.00	1315	17.10	22.50	27.30	28.80	25.10
Y	0.05	25.09	27.23	11.31	10.71	10.75	8.30	6.05	34.37	5.58	7.31	13.03	12.81	6.45
Ga	0.04	21.17	22.74	31.53	31.14	33.91	31.14	15.17	26.28	30.18	30.18	36.08	30.66	18.94
Th	0.02	10.72	11.67	15.80	13.76	32.66	15.55	10.53	5.80	11.68	12.91	18.13	14.65	42.50
U	0.01	1.52	1.79	2.20	2.19	2.61	2.65	2.65	1.75	2.81	2.57	2.24	1.90	3.76
Zr	6.00	132.00	224.00	260.00	224.00	316.00	241.00	147.00	129.00	293.00	275.00	199.00	160.00	83.00
Li	0.40	27.00	27.00	4.70	4.60	6.20	3.70	1.50	6.30	3.40	3.80	5.10	3.80	1.70
Sb	0.04	0.01	0.05	0.10	0.09	0.14	0.06	0.07	0.31	<dl	<dl	0.12	0.04	0.11
Nb	0.03	12.78	15.12	16.33	17.00	20.12	17.70	8.45	7.30	17.40	15.15	18.15	14.77	7.94
Hf	0.14	3.66	5.91	6.93	6.15	8.81	6.44	3.86	3.59	7.66	7.22	5.31	4.43	2.41
Be	0.04	1.89	1.93	2.51	2.43	2.82	2.22	1.16	1.37	2.28	2.45	2.66	2.47	1.47
Cd	0.01	0.14	0.13	0.02	0.02	0.01	0.03	0.05	26.51	0.01	0.02	0.01	0.03	0.03
Mo	0.08	4.05	0.64	1.67	1.81	1.94	1.99	0.96	7.91	1.55	1.40	1.94	2.45	4.17
Sn	0.16	3.23	3.22	4.27	4.31	4.82	4.15	2.45	2.77	3.58	4.37	5.71	3.77	1.40
Tl	0.01	0.52	0.60	0.01	0.08	0.01	0.02	0.01	34.04	0.01	0.01	0.03	0.09	<dl
W	0.05	0.72	0.34	0.44	0.35	0.54	0.51	0.22	0.27	0.59	0.59	0.50	0.27	0.28
Cs	0.01	3.77	4.20	0.15	0.12	0.12	0.25	0.04	0.07	0.12	0.12	0.35	0.17	0.06
Rb	0.23	114.46	134.75	1.79	1.30	1.56	1.97	0.36	1.43	1.00	1.03	2.98	1.75	0.60
Sr	0.60	382.20	336.80	49.20	48.80	45.01	31.20	4.80	13.60	19.80	28.40	54.60	57.50	20.20
Ta	0.02	0.76	0.91	0.93	1.03	1.07	1.02	0.52	0.46	1.03	0.83	1.09	0.86	0.50
Th/U	-	7.05	6.52	7.18	6.28	12.51	5.87	3.97	3.31	4.16	5.02	8.09	7.71	55.92
Th/Co	-	0.39	0.75	5.18	5.07	16.33	5.84	1.45	0.00	4.19	5.87	7.99	4.26	3.53

d.l.: detection limits.

Table 5
Rare-earth element composition of the parent rock and the main constituents of the coarse saprolite (ppm).

REE	d.l.	Parent rock		Coarse saprolite										
		Fresh rock	Sligthly weathered rock	Bottom			Top							
				Whole fraction	Brown material	White veins	Whole fraction	Dark red iron duricrust	Mn-phases	Yellowish brown plates				Dusky red iron duricrust
										(a)	(b)	(c)	(d)	
		CE 01	CE 02	CE 04	CE 07	CE 08	CE 10	CE 09	CE 13	CE 11	CE 12	CE 06	CE 14	CE 05
La	0.04	43.04	44.92	23.95	24.63	20.61	17.47	4.57	166.89	10.91	14.56	25.76	22.48	8.34
Ce	0.12	87.02	86.86	35.92	33.31	117.58	27.00	9.15	5,202	17.15	21.77	39.54	33.40	12.62
Pr	0.01	10.54	10.55	4.41	4.39	3.58	3.72	2.27	40.06	2.48	3.15	5.33	4.47	2.63
Nd	0.06	40.79	41.32	16.79	16.86	13.58	14.20	9.40	123.75	9.61	12.66	20.81	17.42	10.87
Sm	0.01	7.86	7.60	4.08	4.20	3.34	3.39	3.04	26.68	2.42	3.20	5.07	4.46	3.28
Eu	0.03	1.56	1.56	1.08	1.11	0.90	0.88	0.70	9.092	0.64	0.88	1.30	1.25	0.80
Gd	0.01	6.21	6.15	3.88	4.16	3.49	3.06	2.26	15.45	2.09	2.91	4.62	4.44	2.50
Tb	0.002	0.88	0.89	0.56	0.61	0.53	0.44	0.45	3.21	0.32	0.43	0.67	0.64	0.43
Dy	0.01	4.91	5.25	3.12	3.24	2.84	2.48	2.79	17.18	1.82	2.37	3.59	3.62	2.58
Ho	0.003	0.91	0.98	0.51	0.52	0.49	0.41	0.49	3.08	0.30	0.37	0.61	0.61	0.44
Er	0.01	2.50	2.66	1.20	1.21	1.17	1.00	1.48	9.45	0.74	0.90	1.47	1.42	1.24
Tm	0.002	0.35	0.37	0.14	0.14	0.14	0.13	0.25	1.63	0.10	0.12	0.18	0.17	0.20
Yb	0.01	2.22	2.29	0.80	0.78	0.83	0.86	1.95	12.40	0.70	0.74	1.05	0.96	1.42
Lu	0.002	0.32	0.33	0.10	0.09	0.11	0.11	0.26	1.75	0.09	0.09	0.13	0.12	0.19
ΣREE	-	209.10	211.73	96.56	95.24	169.17	75.16	39.06	5632.61	49.38	64.15	110.13	95.45	47.53
ΣLREE	-	190.81	192.81	86.23	84.51	159.59	66.66	29.14	5568.48	43.22	56.22	97.81	83.48	38.53
ΣHREE	-	18.29	18.92	10.34	10.73	9.59	8.50	9.92	64.13	6.16	7.92	12.32	11.10	8.99
a.	-	10.44	10.19	8.34	7.87	16.65	7.84	2.94	86.83	7.01	7.09	7.94	6.97	4.28
Ce/Ce^* (1)	-	0.99	0.97	-	-	-	-	-	-	-	-	-	-	-
Eu/Eu^* (1)	-	0.68	0.69	-	-	-	-	-	-	-	-	-	-	-
Ce/Ce^* (2)	-	-	-	0.86	0.78	3.35	0.82	0.69	15.57	0.81	0.79	0.83	0.82	0.66
Eu/Eu^* (2)	-	-	-	1.22	1.19	1.18	1.23	1.20	2.01	1.40	1.30	1.20	1.25	1.25
$(La/Yb)_N$	-	13.19	13.35	1.51	1.63	1.29	1.05	0.12	0.69	0.80	1.02	1.26	1.21	0.30

d.l.: detection limits.
a. = LREE/ HREE.
Ce anomaly = $(Ce/Ce^*)(1) = (Ce_{orthogneissl}/Ce_{chondrite})/(La_{orthogneiss}/La_{chondrite})^{0.5}(Pr_{orthogneiss}/Pr_{chondrite})^{0.5}$.
Eu anomaly = $(Eu/Eu^*)(1) = (Eu_{orthogniess}/Eu_{chondrite})/(Sm_{orthogniess}/Sm_{chondrite})^{0.5}(Gd_{orthogneiss}/Gd_{c\ hondrite})^{0.5}$.
Ce anomaly = $(Ce/Ce^*)(2) = (Ce_{weathered\ sample}Ce_{orthogneiss})/(La_{weathered\ sample}/La_{orthogneiss})^{0.5}(Pr_{weathered\ sample}/Pr_{orthogneiss})^{0.5}$.
Eu anomaly = $(Eu/Eu^*)(2) = (Eu_{weathered\ sampe}/Eu_{orthogneiss})/(Sm_{weathered\ sample}/Sm_{orthogneiss})^{0.5}(Gd_{weathered\ sample}/Gd_{orthogneiss})^{0.5}$.
For rock samples: $(La/Yb)_N = (La_{orthogneiss}/La_{chondrite})/(Yb_{orthogneiss}/Yb_{chondrite})$.
For weathered samples: $(La/Yb)_N = (La_{weathered\ sample}/La_{orthogneiss})/(Yb_{weathered\ sample}/Yb_{orthogneiss})$.

Table 6
Geochemical balance evaluation of major elements in the coarse saprolite by isovolumetric method (%).

	Coarse saprolite										
	Bottom			Top							
	Whole fraction	Brown material	White veins	Whole fraction	Dark red iron duricrust	Mn-phases	Yellowish brown plates				Dusky red iron duricrust
							(a)	(b)	(c)	(d)	
Depth (m)	-	+ 0.10	+ 0.40	-	+1.70	+1.70	+1.70	+1.80	+2.10	+2.40	+2.50
Ref. code	CE 04	CE 07	CE 08	CE 10	CE 09	CE 13	CE 11	CE 12	CE 06	CE 14	CE 05
Si	-36.07	-53.96	-42.37	-35.28	-45.28	-46.65	-35.62	-39.18	-45.60	-37.13	-58.69
Al	-0.79	-27.47	-13.14	**6.19**	-11.87	-0.44	**8.48**	**4.87**	-5.24	-3.87	-31.47
Fe	-53.82	-64.54	-82.48	-25.31	**849.56**	**67.64**	-13.64	-39.91	-61.44	-38.73	**433.42**
Mn	-95.10	-96.44	-95.79	-94.72	-90.32	**30482**	-94.57	-94.95	-95.64	-95.06	-93.65
Mg	-	-	-	-99.84	-98.86	-96.00	-98.55	-98.81	-	-99.85	-99.25
Ca	-99.59	-99.80	-99.77	-99.71	-99.47	-99.25	-99.70	-99.72	-99.76	-99.73	-99.65
Na	-	-	-	-99.50	-	-95.25	-99.48	-99.52	-	-99.53	-
K	-99.09	-99.51	-99.22	-99.27	-99.55	-86.63	-99.50	-99.53	-99.19	-98.86	-99.71
Ti	-5.53	-30.85	-12.20	**7.13**	**7.89**	-79.36	**16.45**	**5.36**	-5.26	-28.06	-39.19
P	-75.08	-81.89	-80.96	-79.10	-83.58	-84.69	-84.64	-82.87	-75.34	-74.89	-64.09
LOI	**1288**	**909**	**1075**	**1492**	**2541**	**3281**	**1617**	**1525**	**1241**	**1333**	**1867**

Table 7
Geochemical balance evaluation of trace elements in the coarse saprolite by isovolumetric method (%).

	Coarse saprolite										
	Bottom			Top							
	Whole fraction	Brown material	White veins	Whole fraction	Dark red iron duricrust	Mn-phases	Yellowish brown plates				Dusky red iron duricrust
							(a)	(b)	(c)	(d)	
Depth (m)	-	+ 0.10	+ 0.40	-	+1.70	+1.70	+1.70	+1.80	+2.10	+2.40	+2.50
Ref. code	CE 04	CE 07	CE 08	CE 10	CE 09	CE 13	CE 11	CE 12	CE 06	CE 14	CE 05
Cr	-28.78	-43.40	-46.13	-8.81	-13.90	-55.38	-12.81	-25.61	-23.43	-44.72	**390.50**
Ni	-84.17	-88.94	-89.44	-78.96	-50.84	**10.88**	-78.01	-80.96	-82.15	-83.97	-82.21
Co	-92.89	-95.41	-95.99	-93.32	-66.46	**7275**	-92.79	-94.71	-95.29	-91.92	-83.77
Zn	-75.74	-83.26	-80.72	-64.69	**85.81**	**170.61**	-58.28	-68.10	-71.37	-67.60	**12.48**
Sc	-13.89	-34.01	-20.71	**3.38**	**141.73**	**86.79**	**15.60**	**0.75**	-21.37	-9.93	**128.99**
Cu	-68.74	-74.27	-70.56	-33.49	-24.74	**923.61**	-19.02	-46.16	-64.61	-41.69	**77.03**
V	**0.13**	-32.53	-22.68	**20.52**	**163.50**	**9.93**	**29.25**	**5.83**	-1.74	-22.36	**181.00**
Ba	-77.78	-83.66	-81.38	-86.38	-97.44	**6526**	-92.67	-88.66	-80.16	-76.14	-90.42
Pb	**7.80**	-22.89	-27.75	-5.77	**48.08**	**9991**	-21.04	-3.42	**1.20**	**20.81**	**35.49**
Y	-71.29	-80.25	-76.55	-77.29	-69.65	**60.84**	-84.29	-80.87	-70.55	-67.23	-78.77
Ga	-5.15	-31.94	-12.34	**0.99**	-9.80	**45.75**	**0.71**	-6.38	-3.34	-7.05	-26.11
Th	-6.13	-40.60	**66.74**	-0.43	**23.62**	-36.47	-23.03	-20.90	-4.07	-12.31	**227.44**
U	-7.61	-33.21	-5.65	**20.23**	**120.09**	**35.47**	**31.17**	11.32	-16.07	-19.68	**105.02**
Zr	**25.43**	-21.48	**31.01**	**25.35**	**40.17**	**14.74**	**56.81**	**36.82**	-14.50	-22.21	-48.07
Li	-88.91	-92.12	-87.73	-90.59	-93.01	-72.60	-91.10	-90.76	-89.29	-90.97	-94.80
Sb	**961.36**	**594.03**	**1177**	**587**	**1368**	**5966**	-	-	**1034**	**327.86**	**1,414**
Nb	-18.66	-38.47	-13.89	-4.97	-16.75	-32.95	-3.83	-22.15	-19.49	-25.85	-48.69
Hf	**20.58**	-22.25	**31.73**	**20.81**	**32.75**	**15.17**	**47.86**	**29.55**	-17.71	-22.32	-45.62
Be	-15.43	-40.51	-18.34	-19.36	-22.75	-14.89	-14.78	-14.87	-20.18	-16.13	-35.77
Cd	-90.20	-95.15	-95.02	-86.08	-56.87	**21667**	-93.58	-93.11	-94.45	-86.54	-80.36
Mo	-73.74	-79.32	-73.79	-66.26	-70.16	**129.32**	-72.96	-77.30	-72.83	-61.18	-14.97
Sn	-15.81	-38.26	-18.33	-11.79	-4.53	**0.69**	-21.70	-11.15	**0.26**	-25.09	-64.20
Tl	-98.52	-99.37	-98.94	-97.35	-98.30	**7616**	-99.05	-99.37	-96.72	-89.34	-
W	-61.08	-77.51	-58.96	-51.37	-61.54	-55.97	-42.11	-46.19	-60.61	-75.93	-67.88
Cs	-97.45	-98.59	-98.21	-95.42	-98.73	-97.79	-97.71	-97.84	-94.68	-97.19	-98.73
Rb	-99.00	-99.47	-99.25	-98.82	-99.60	-98.53	-99.38	-99.41	-98.52	-99.02	-99.57
Sr	-91.80	-94.09	-93.56	-94.40	-98.42	-95.82	-96.34	-95.12	-91.90	-90.34	-95.64

Table 8
Geochemical balance evaluation of rare-earth elements in the coarse saprolite by isovolumetric method (%).

	Coarse saprolite										
	Bottom			Top							
	Whole fraction	Brown material	White veins	Whole fraction	Dark red iron duricrust	Mn-phases	Yellowish brown plates				Dusky red iron duricrust
							(a)	(b)	(c)	(d)	
Depth (m)	-	+ 0.10	+ 0.40	-	+1.70	+1.70	+1.70	+1.80	+2.10	+2.40	+2.50
Ref. code	CE 04	CE 07	CE 08	CE 10	CE 09	CE 13	CE 11	CE 12	CE 06	CE 14	CE 05
La	-64.56	-73.52	-73.79	-72.13	-86.64	**355.28**	-82.09	-77.78	-66.05	-66.48	-84.00
Ce	-73.71	-82.29	-26.05	-78.70	-86.76	**6919**	-86.08	-83.57	-74.23	-75.37	-88.02
Pr	-73.37	-80.73	-81.43	-75.81	-72.85	**346.26**	-83.37	-80.36	-71.35	-72.79	-79.43
Nd	-73.79	-80.99	-81.78	-76.10	-70.99	**256.21**	-83.36	-79.62	-71.06	-72.59	-77.99
Sm	-66.98	-75.26	-76.76	-70.36	-51.28	**298.58**	-78.22	-73.26	-63.39	-63.58	-65.56
Eu	-55.84	-67.00	-68.37	-61.07	-43.40	**584.75**	-70.91	-62.85	-52.63	-48.75	-57.73
Gd	-60.15	-69.02	-69.23	-66.10	-54.09	**192.26**	-76.26	-69.25	-57.73	-54.08	-66.74
Tb	-59.40	-68.30	-67.34	-65.63	-35.85	**326.70**	-74.40	-68.09	-57.16	-53.34	-59.41
Dy	-59.47	-69.49	-68.38	-65.37	-28.39	**310.93**	-73.75	-68.29	-58.56	-52.62	-56.61
Ho	-63.83	-73.31	-70.67	-68.90	-32.27	**299.72**	-76.97	-72.86	-61.71	-57.10	-59.66
Er	-69.33	-77.64	-74.77	-72.54	-25.69	**343.59**	-79.03	-76.44	-66.63	-63.44	-59.10
Tm	-74.16	-81.89	-77.64	-73.91	-9.37	**445.47**	-79.01	-78.23	-71.64	-69.56	-53.99
Yb	-76.91	-83.80	-79.63	-73.34	**10.60**	**556.56**	-77.76	-78.20	-73.11	-72.24	-47.03
Lu	-79.31	-86.72	-81.01	-75.53	**1.25**	**547.44**	-79.05	-80.53	-76.74	-76.11	-51.80

Table 9
Mass balance calculations of major elements in the coarse saprolite by isovolumetric method (kg/m^3).

	Coarse saprolite										
	Bottom			Top							
	Whole fraction	Brown material	White veins	Whole fraction	Dark red iron duricrust	Mn-phases	Yellowish brown plates				Dusky red iron duricrust
							(a)	(b)	(c)	(d)	
Depth (m)	-	+ 0.10	+ 0.40	-	+1.70	+1.70	+1.70	+1.80	+2.10	+2.40	+2.50
Ref. code	CE 04	CE 07	CE 08	CE 10	CE 09	CE 13	CE 11	CE 12	CE 06	CE 14	CE 05
Si	-446.32	-667.73	-524.23	-436.54	-560.33	-577.26	-440.74	-484.82	-564.19	-459.49	-726.24
Al	-2.28	-79.17	-37.87	**17.85**	-34.22	-1.26	**24.45**	**14.05**	-15.09	-11.14	-90.69
Fe	-76.37	-91.59	-117.05	-35.92	**1205**	**95.98**	-19.36	-56.63	-	-54.96	**615.05**
Mn	-2.49	-2.52	-2.50	-2.48	-2.36	**796.48**	-2.47	-2.48	-2.50	-2.48	-2.45
Mg	-	-	-	-88.30	-87.43	-84.90	-87.16	-87.38	-88.44	-88.31	-87.78
Ca	-94.29	-94.49	-94.45	-94.40	-94.17	-93.96	-94.39	-94.41	-94.44	-94.41	-94.34
Na	-	-	-	-54.40	-	-52.08	-54.39	-54.41	-	-54.41	-
K	-55.97	-56.20	-56.04	-56.07	-56.23	-48.93	-56.20	-56.22	-56.03	-55.84	-56.32
Ti	-1.01	-5.64	-2.23	**1.31**	**1.44**	-14.52	**+3.01**	**+0.98**	-0.96	-5.13	-7.17
P	-3.47	-3.79	-3.74	-3.66	-3.86	-3.92	-3.91	-3.83	-3.48	-3.46	-2.96
LOI	**11.29**	**78.59**	**92.89**	**128.94**	**217.29**	**284.23**	**139.75**	**131.81**	**107.30**	**115.20**	**161.34**

Table 10
Mass balance calculations of trace elements in the coarse saprolite by isovolumetric method (g/m^3).

	Coarse saprolite										
	Bottom			Top							
	Whole fraction	Brown material	White veins	Whole fraction	Dark red iron duricrust	Mn-phases	Yellowish brown plates				Dusky red iron duricrust
							(a)	(b)	(c)	(d)	
Depth (m)	-	+ 0.10	+ 0.40	-	+1.70	+1.70	+1.70	+1.80	+2.10	+2.40	+2.50
Ref. code	CE 04	CE 07	CE 08	CE 10	CE 09	CE 13	CE 11	CE 12	CE 06	CE 14	CE 05
Cr	-160	-241	-256	-49	-77	-308	-71	-142	-130	-248	**2 169**
Ni	-143	-151	-152	-134	-86	**18**	-134	-138	-140	-143	-140
Co	-51	-52	-53	-51	-36	**3995**	-51	-52	-52	-50	-46
Zn	-160	-176	-170	-137	**181**	**360**	-123	-144	-151	-143	**26**
Sc	-5	-12	-7	**1**	**50**	**31**	**6**	0	-8	-4	**46**
Cu	-53	-57	-54	-26	-19	**711**	-15	-36	-50	-32	**59**
V	0	-88	-61	**56**	**443**	**27**	**79**	**16**	-5	-61	**491**
Ba	-1432	-1540	-1498	-1590	-1794	**120147**	-1706	-1632	**1476**	-1402	-1665
Pb	**2**	-7	-9	-2	**15**	**3073**	-6	-1	0	**6**	**+11**
Y	-36	-40	-39	-39	-35	**31**	-43	-41	-36	-34	-40
Ga	-2	-14	-5	0	-4	**19**	0	-3	-1	-3	-11
Th	-1	-9	**14**	0	**5**	-8	-5	-5	-1	-3	**49**
U	0	-1	0	**1**	**4**	**1**	**1**	0	0	-1	**+3**
Zr	**67**	-57	**82**	**67**	**107**	**39**	**51**	**98**	-38	-59	-128
Li	-48	-50	-47	-49	-50	-39	-49	-49	-48	-49	-51
Nb	-5	-10	-4	-1	-4	-8	-1	-6	-5	-7	-13
Hf	**2**	-2	**2**	**2**	**2**	**1**	**4**	**2**	-1	-2	-3
Be	-1	-2	-1	-1	-1	-1	-1	-1	-1	-1	-1
Mo	-6	-6	-6	-5	-6	**11**	-6	-6	-6	-5	-1
Sn	-1	-2	-1	-1	0	0	-1	-1	0	-2	-4
Tl	-1	1	-1	-1	-1	**79**	-1	-1	-1	-1	-
W	-1	-1	-1	-1	-1	-1	-1	-1	-1	-1	-1
Cs	-7	-7	-7	-7	-7	-7	-7	-7	-7	-7	-7
Rb	-228	-229	-228	-227	-229	-227	-229	-229	-227	-228	-229
Sr	-705	-723	-719	-725	-756	-736	-740	-731	-706	-694	-735

Table 11
Mass balance calculations of rare-earth elements in the coarse saprolite by isovolumetric method (g/m^3).

	Coarse saprolite										
	Bottom			Top							
	Whole fraction	Brown material	White veins	Whole fraction	Dark red iron duricrust	Mn-phases	Yellowish brown plates				Dusky red iron duricrust
							(a)	(b)	(c)	(d)	
Depth (m)	-	+ 0.10	+ 0.40	-	+1.70	+1.70	+1.70	+1.80	+2.10	+2.40	+2.50
Ref. code	CE 04	CE 07	CE 08	CE 10	CE 09	CE 13	CE 11	CE 12	CE 06	CE 14	CE 05
La	-56	-64	-64	-62	-75	**307**	-71	-67	-57	-58	-73
Ce	-129	-144	-46	-138	-52	**12102**	-151	-146	-130	-132	-154
Pr	-16	-17	-16	-16	-15	**73**	-18	-17	-15	-15	-17
Nd	-60	-66	-67	-62	-58	**210**	-68	-65	-58	-60	-64
Sm	-11	-12	-12	-11	-8	**47**	-12	-12	-10	-10	-10
Eu	-2	-2	-2	-2	-1	**18**	-2	-2	-2	-2	-2
Gd	-8	-9	-9	-8	-7	**24**	-10	-9	-7	-7	-8
Tb	-1	-1	-1	-1	-1	**6**	-1	-1	-1	-1	-1
Dy	-6	-7	-7	-6	-3	**31**	-7	-7	-6	-5	-6
Ho	-1	-1	-1	-1	-1	**5**	-1	-1	-1	-1	-1
Er	-3	-4	-4	-4	-1	**17**	-4	-4	-3	-3	-3
Tm	-1	-1	-1	-1	0	**3**	-1	-1	-1	0	0
Yb	-3	-4	-4	-3	0	**25**	-3	-3	-3	-3	-2
Lu	-1	-1	-1	0	0	**3**	-1	-1	0	0	0

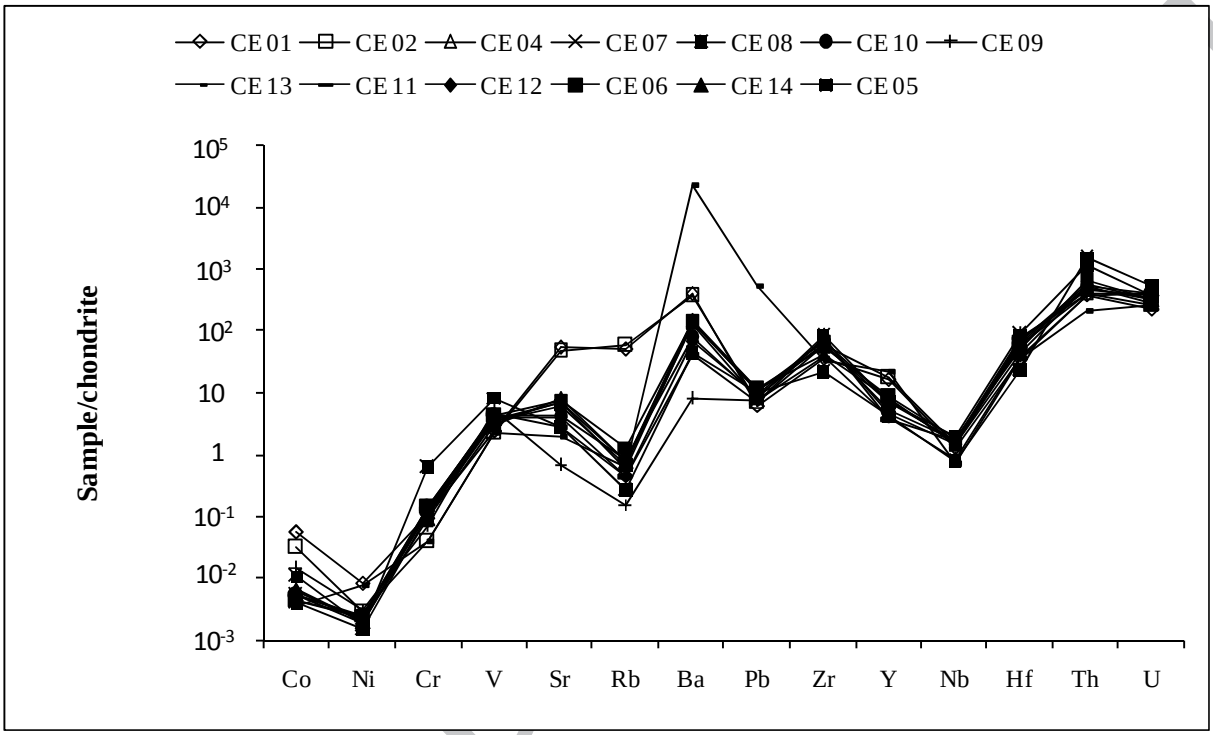

Figure 3

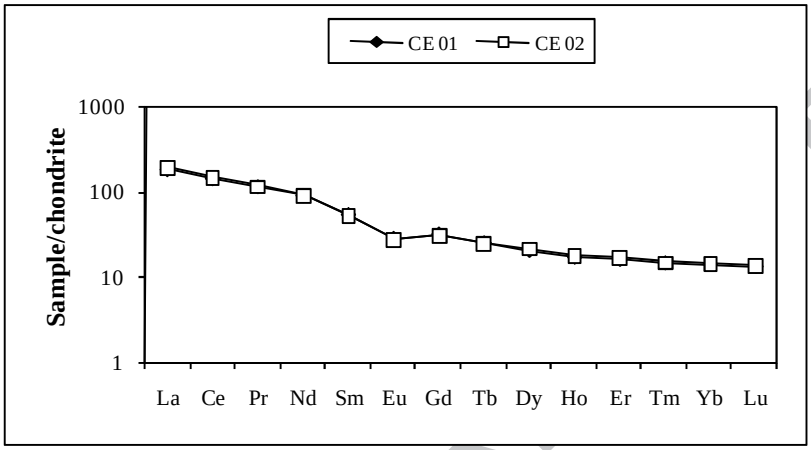

Figure 4

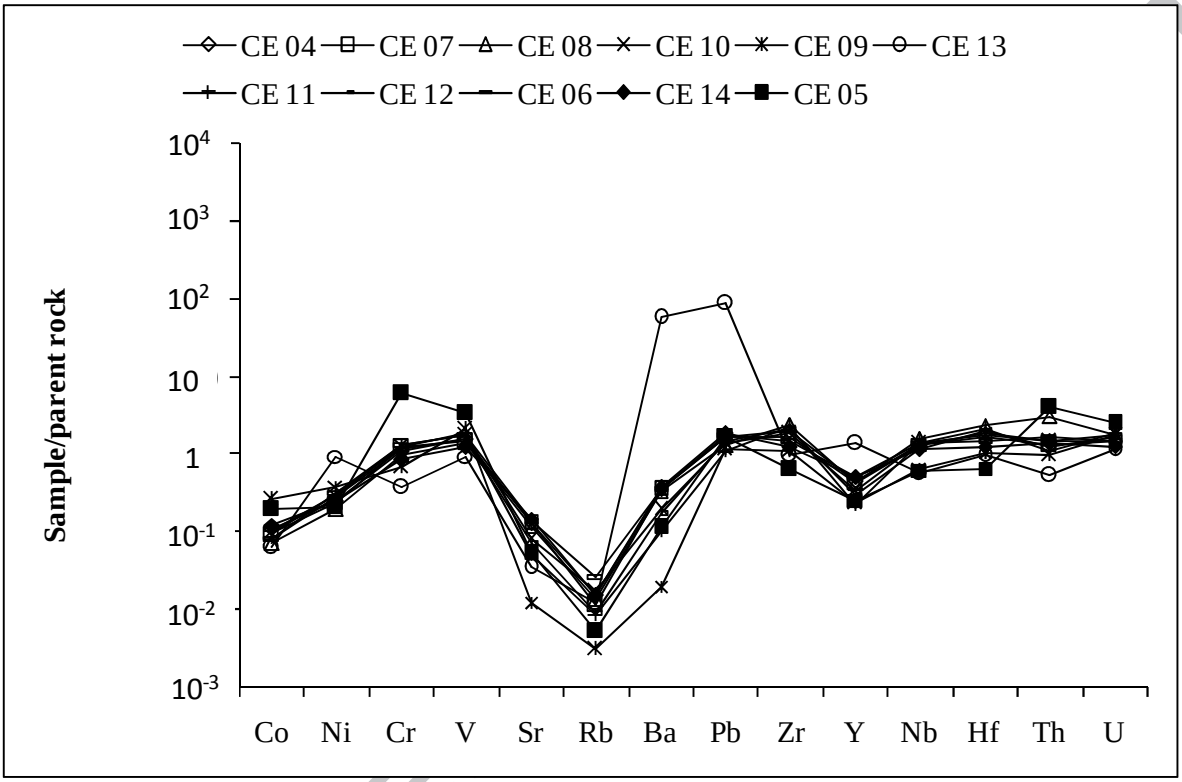

Figure 6

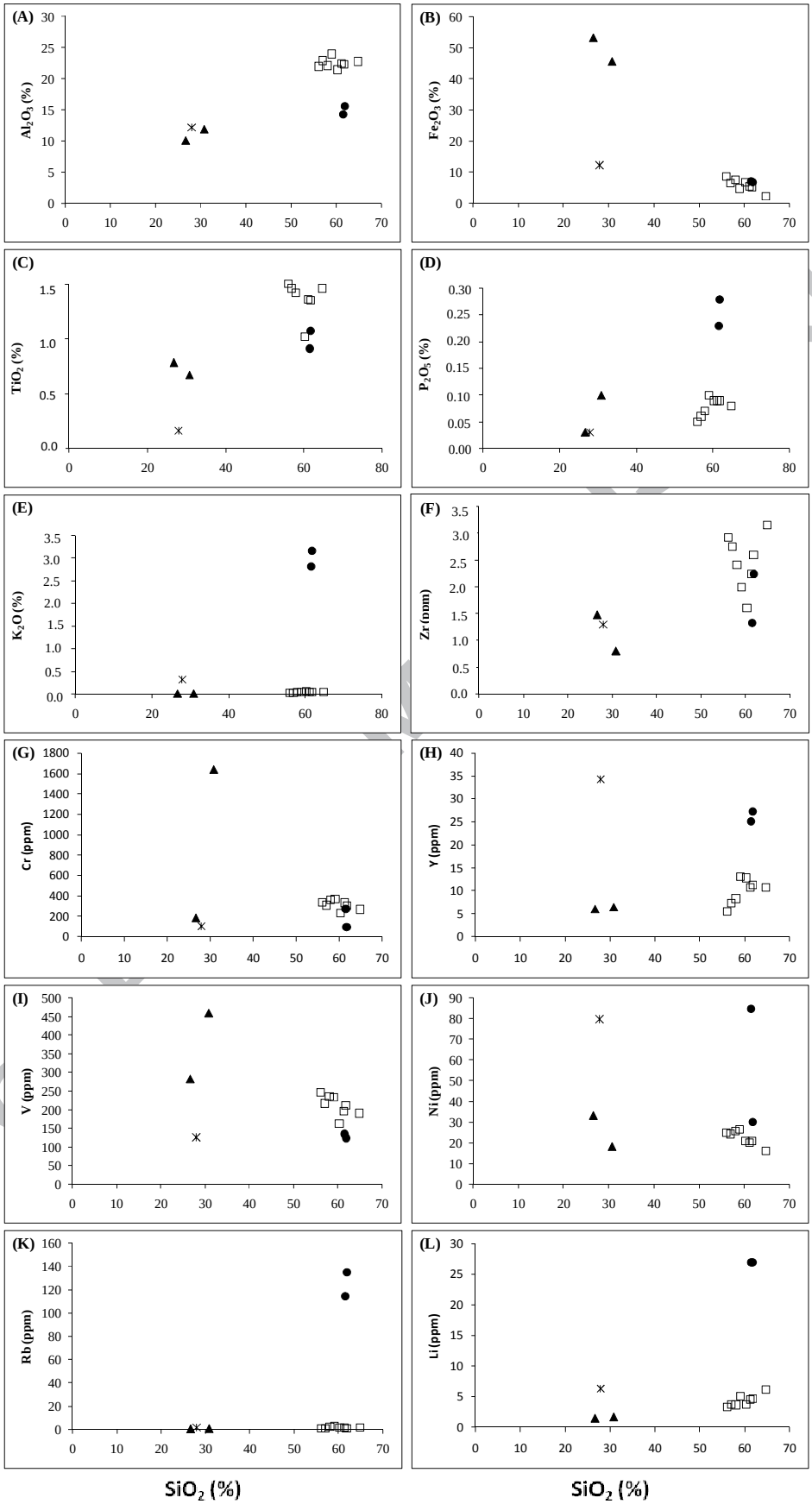

Figure 7

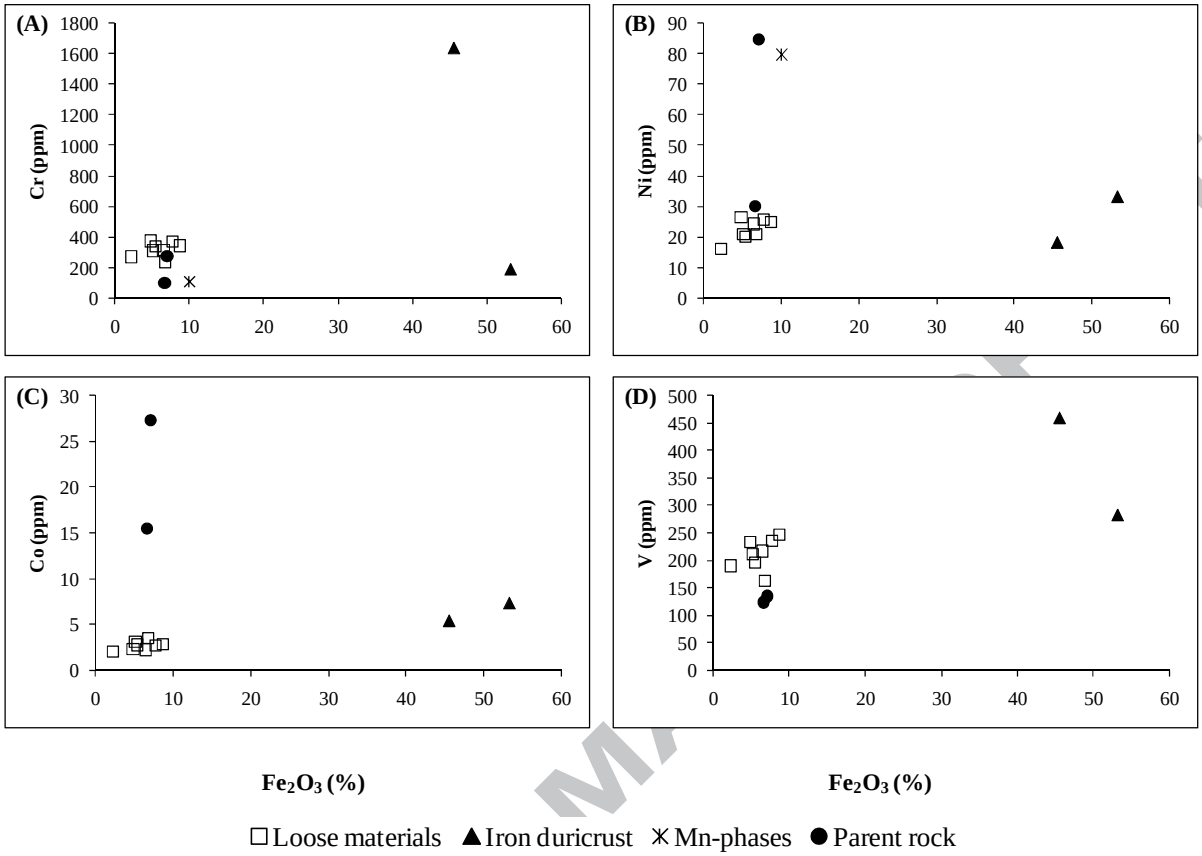

Figure 8

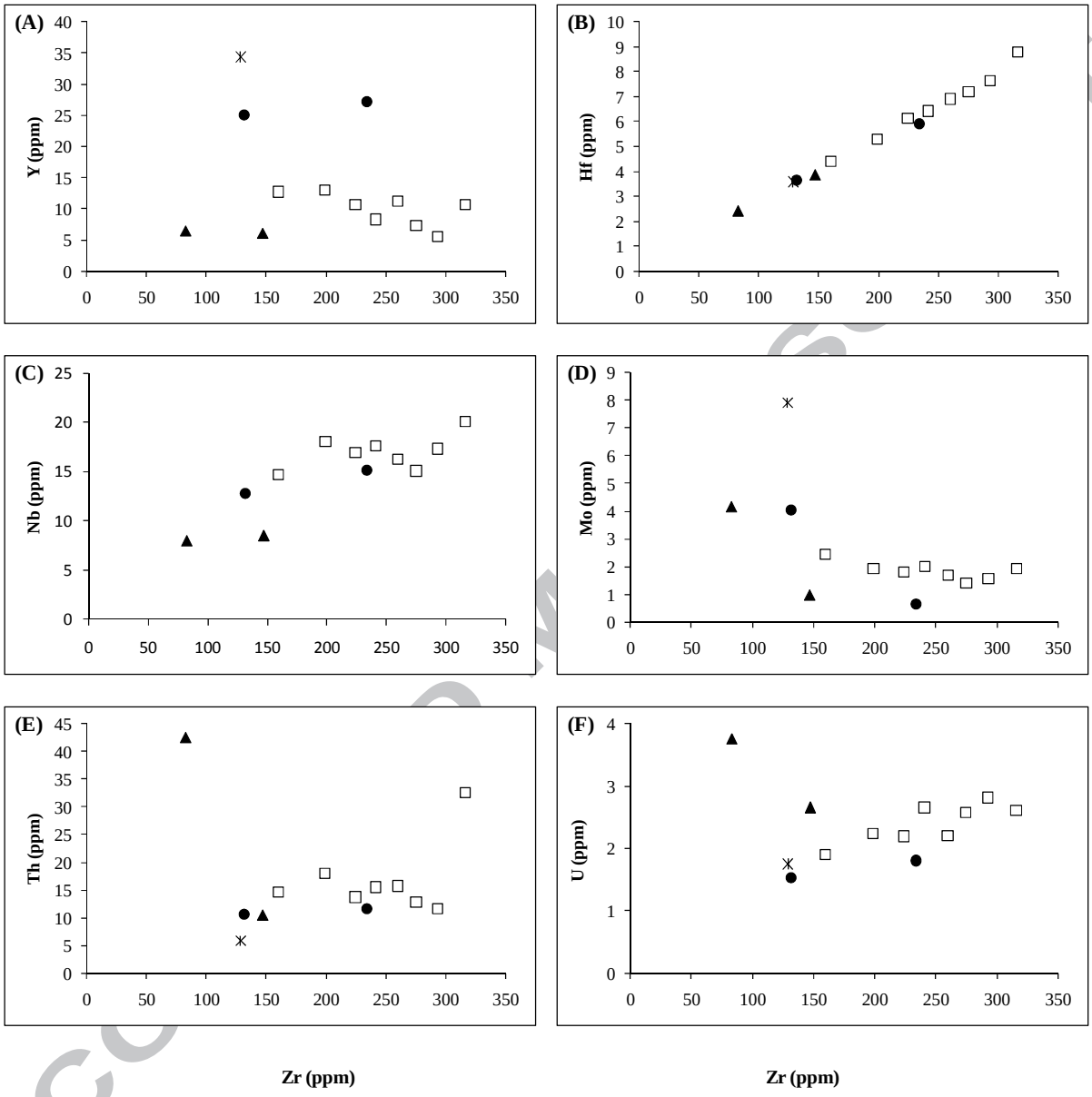

Figure 9

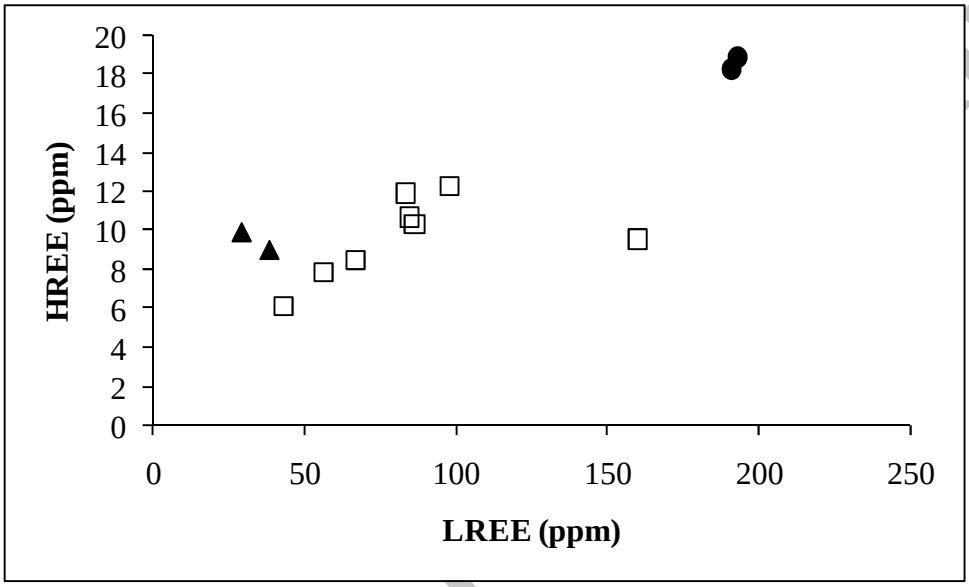

Figure 10

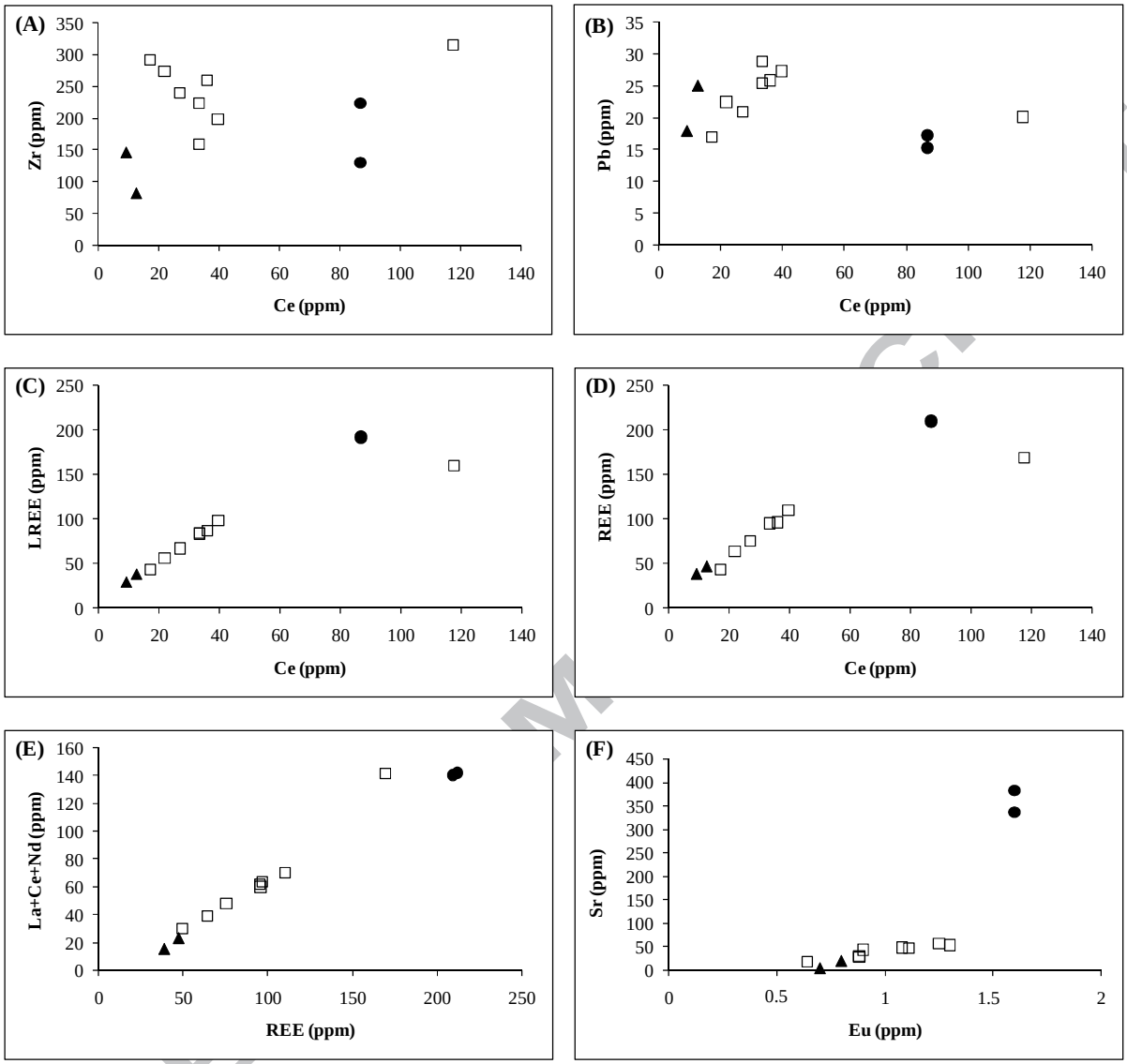

Figure 11

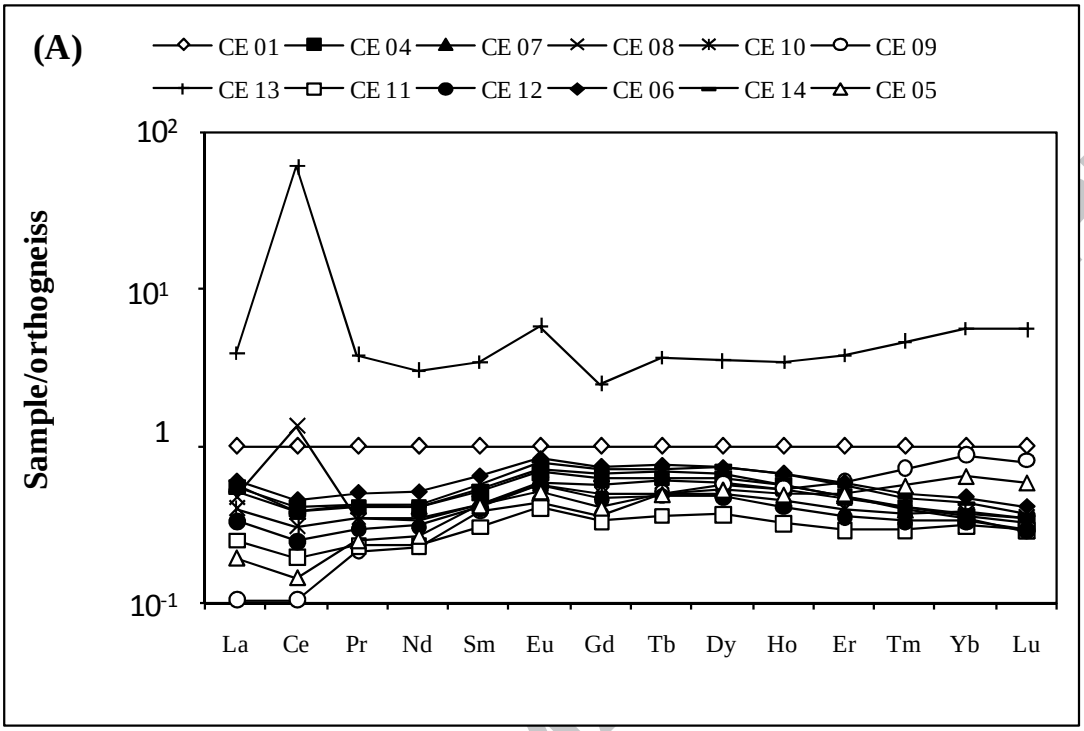

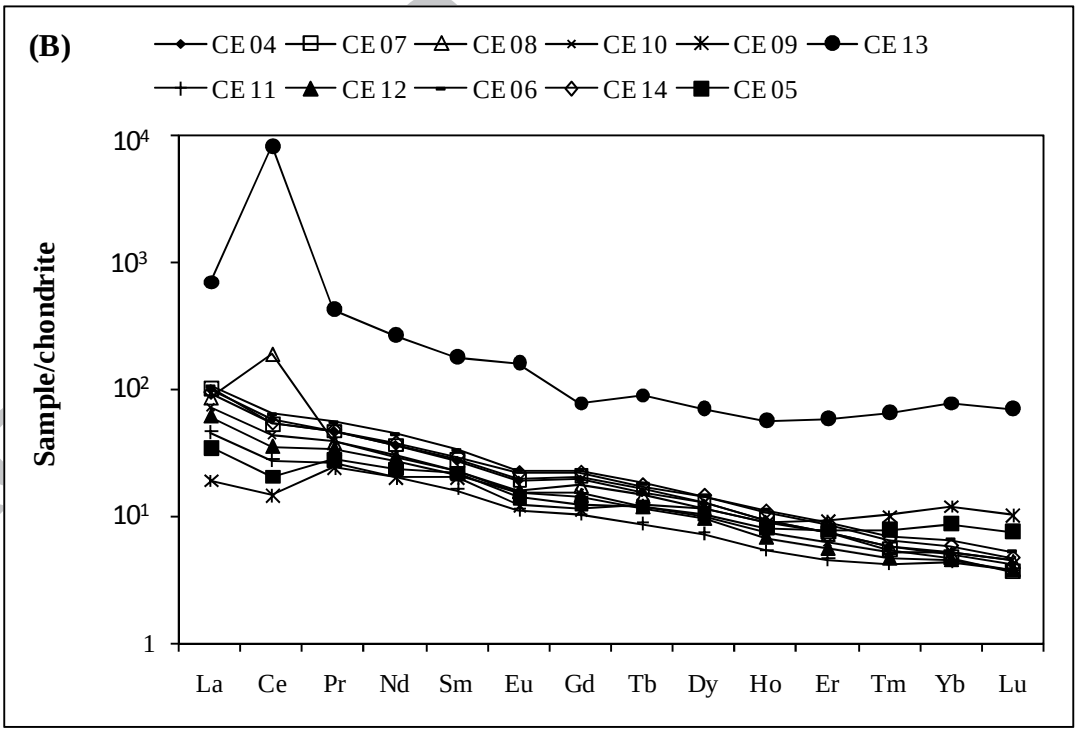

Figure 12

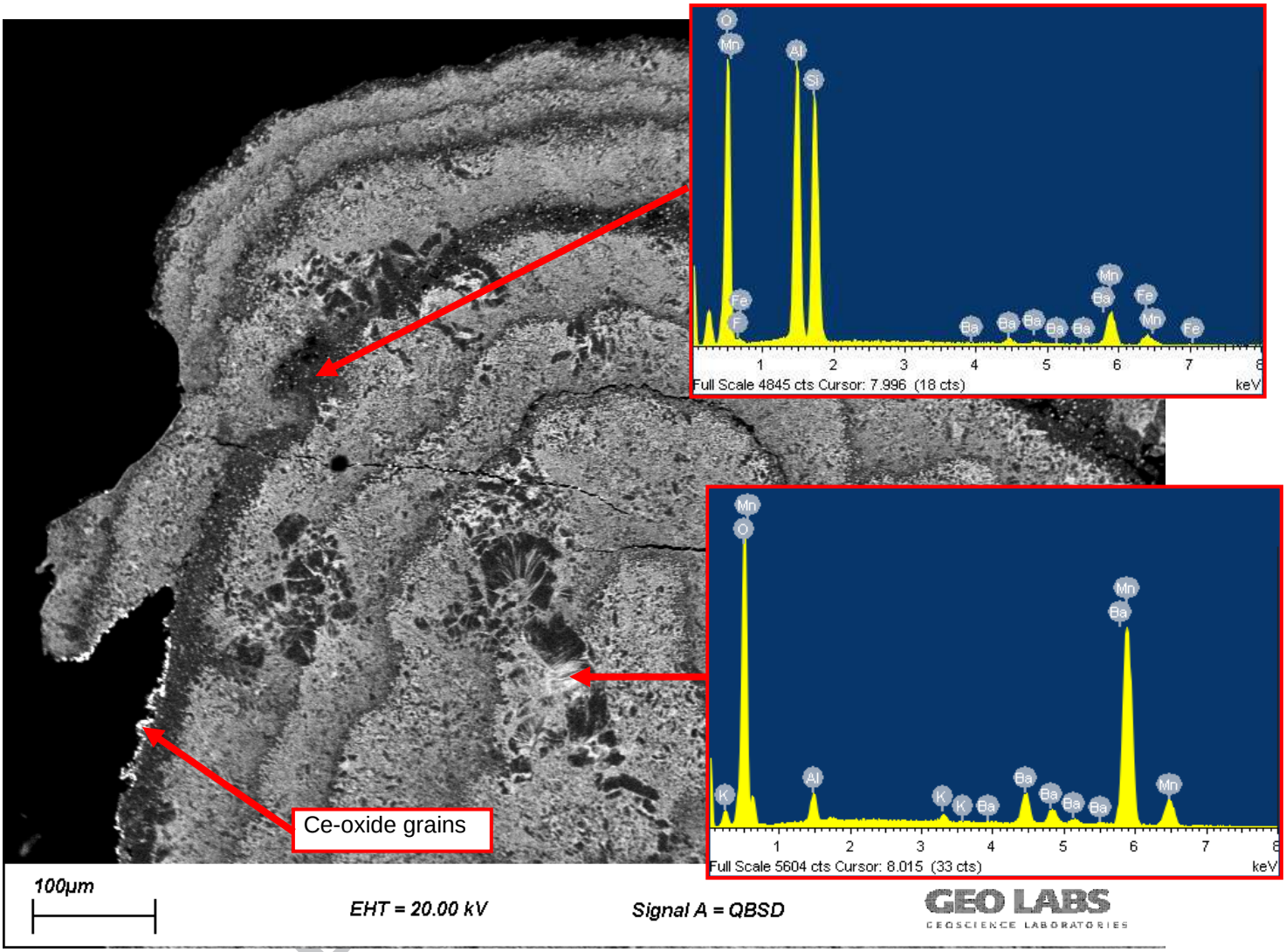

Figure 13

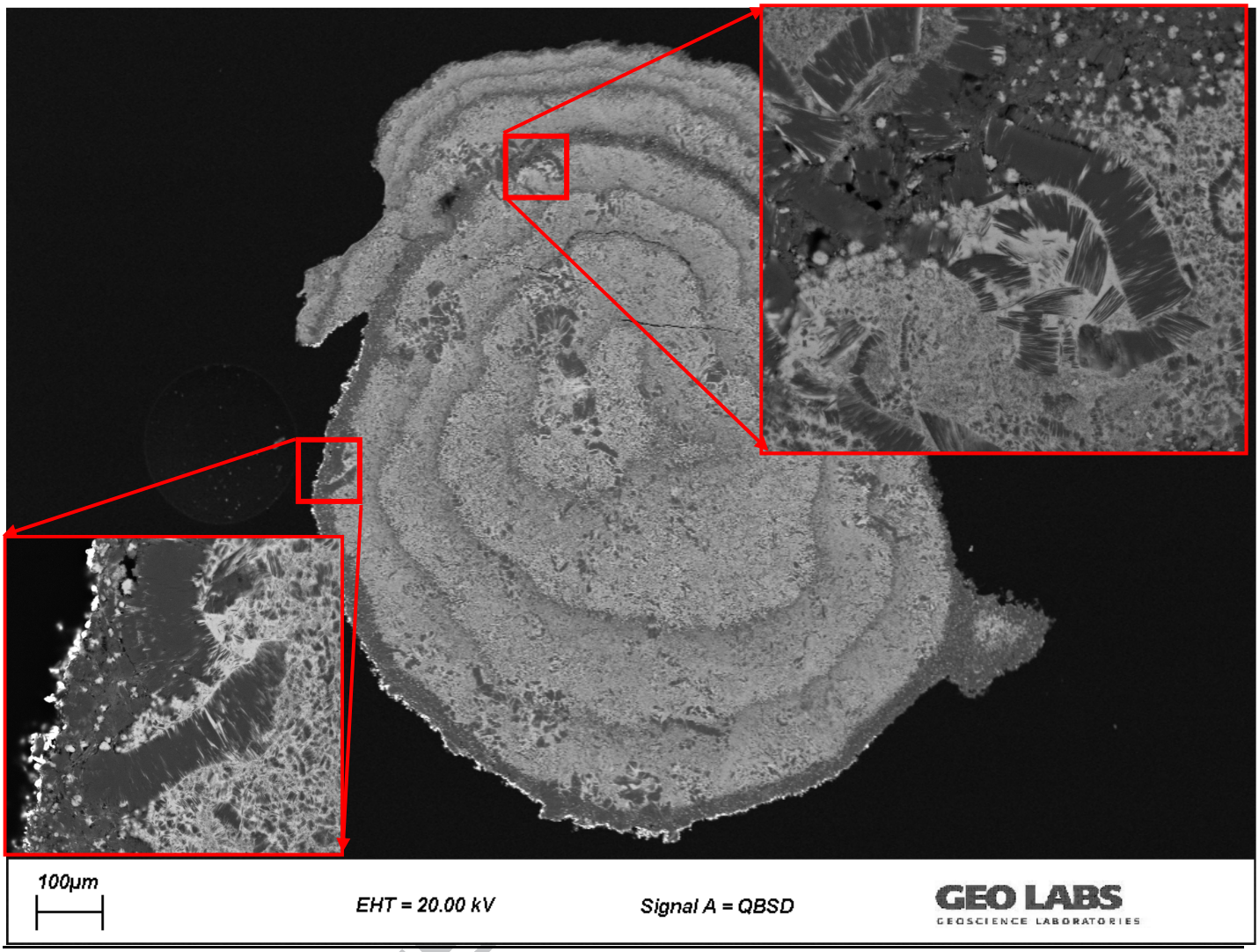

Figure 14

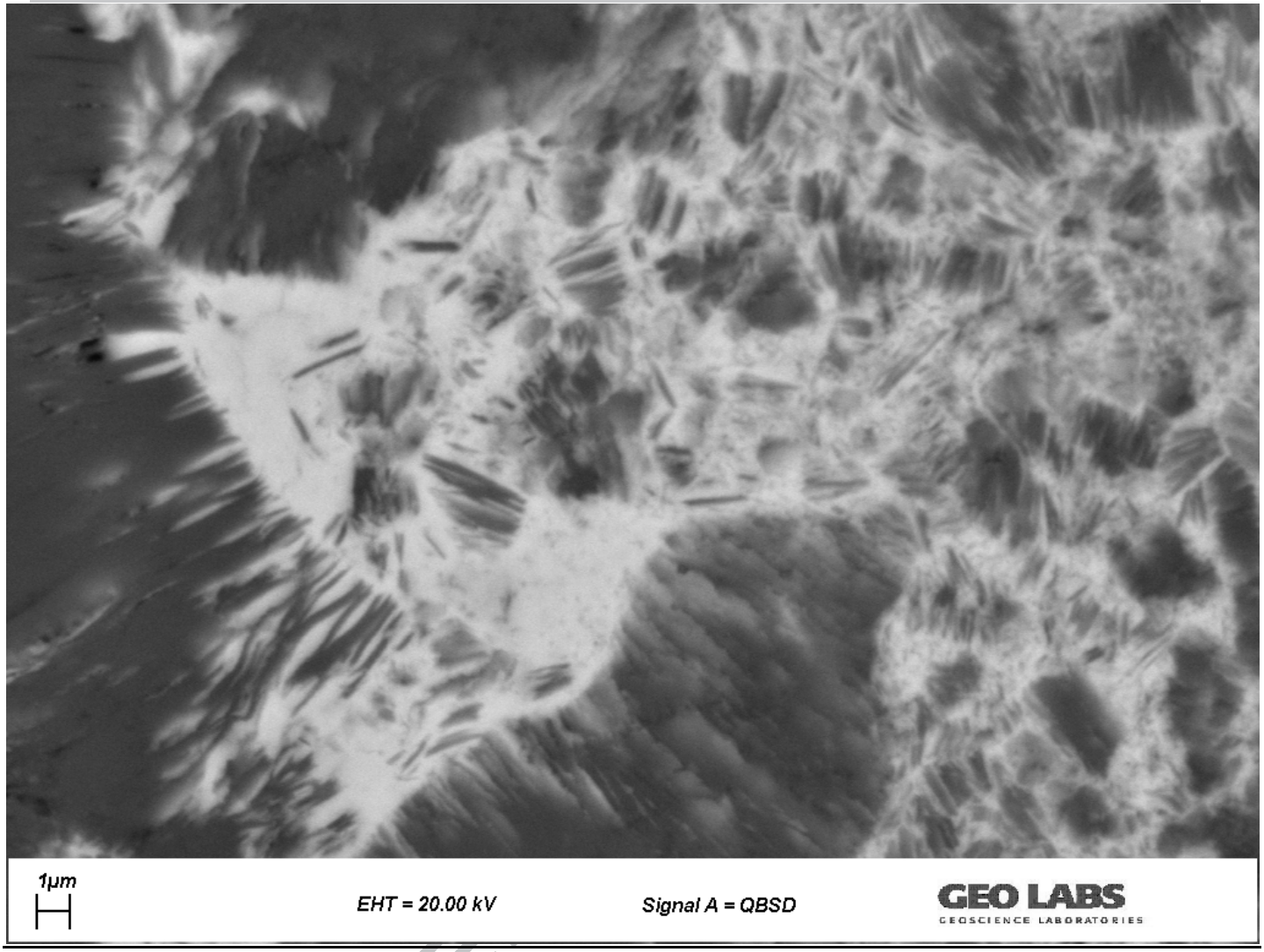

Figure 15

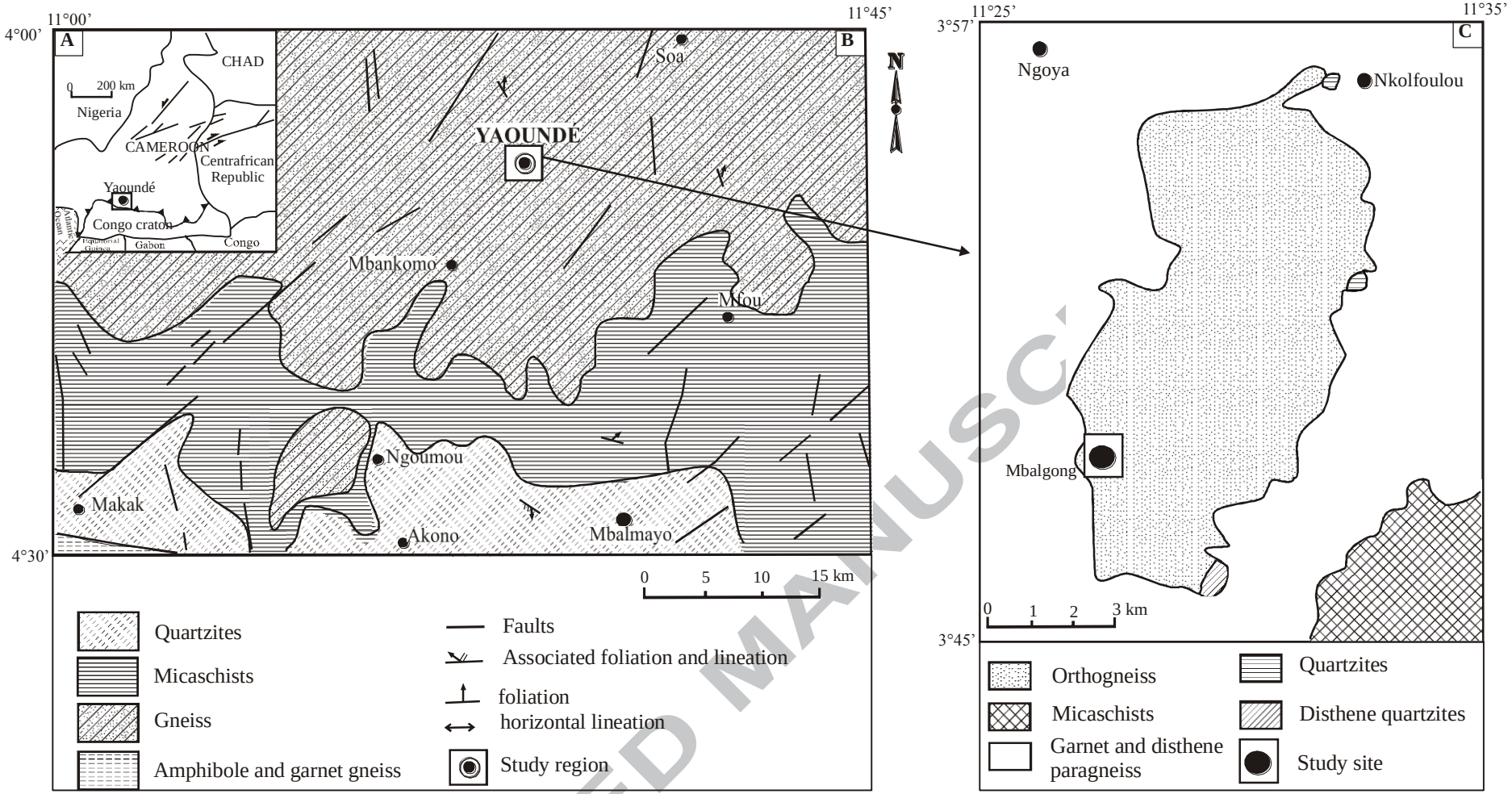

Fig. 1

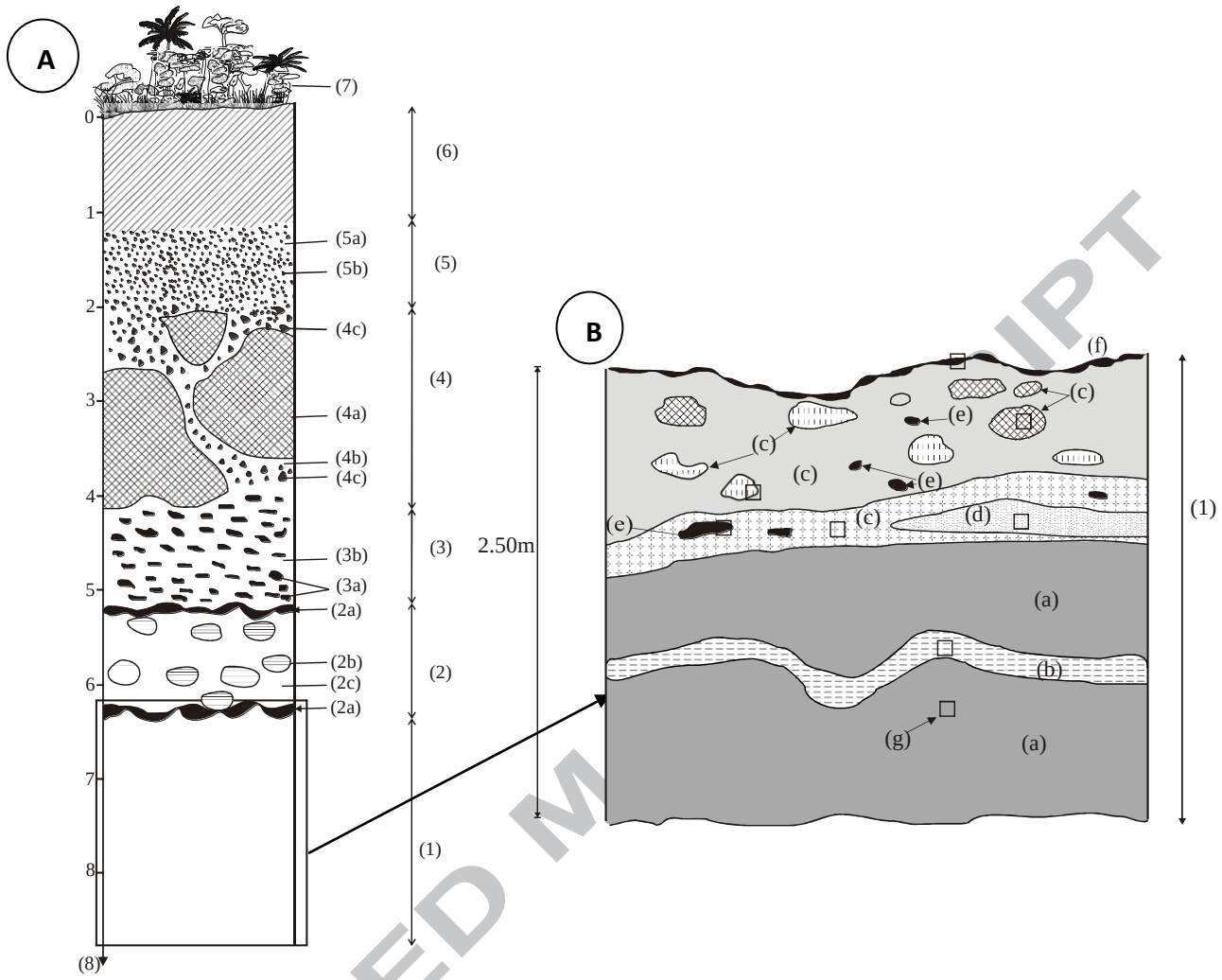

1. coarse saprolite (a. brown materials; b. white veins; c. yellowish brown plates; d. dark red iron duricrust; e. black plates; f. dusky red iron duricrust; g. sample location); 2. fine saprolite (2a: iron duricrust (plates); 2b: plates with relic structure; 2c: patched materials); 3. lower nodular horizon (3a: flattened nodules with relic structure; 3b: dark red matrix); 4. iron duricrust horizon (4a: metric blocks of the nodular iron duricrust; 4b: red matrix; 4c. nodules); 5. upper nodular horizon (5a: red matrix; 5b: nodules); 6. clayey loose horizon; 7. vegetation; 8. Depth.

Figure 2

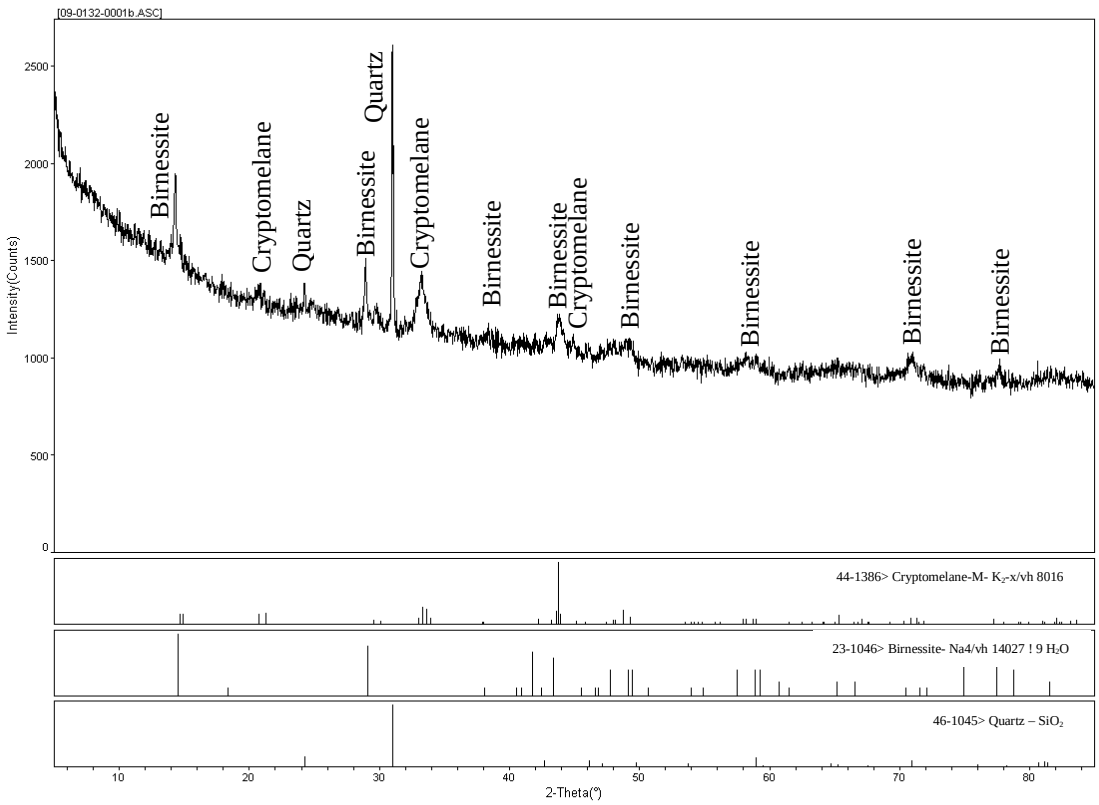

Figure 5